Alma Mater Studiorum - University of Bologna

SCHOOL OF SCIENCE
Department of Industrial Chemistry
"Toso Montanari"

Master Degree in

Industrial Chemistry

Class LM-71 - Science and Technology in Industrial Chemistry

Synthesis, characterization and formulation of a cathode active material: Copper nitroprusside

Experimental Thesis

CANDIDATE

Angelo Mullaliu

SUPERVISOR

Illustrious Professor Marco Giorgetti

CO-SUPERVISOR

Illustrious Professor Lorenzo Stievano

First Session

Academic Year 2014-2015

"Wer nicht mehr liebt und nicht mehr irrt, der lasse sich begraben."

Johann Wolfgang von Goethe

Abstract

Nowadays, rechargeable Li-ion batteries play an important role in portable consumer devices. Formulation of such batteries is improvable by researching new cathodic materials that present higher performances of cyclability and negligible efficiency loss over cycles.

Goal of this work was to investigate a new cathodic material, copper nitroprusside, which presents a porous 3D framework. Synthesis was carried out by a low-cost and scalable co-precipitation method. Subsequently, the product was characterized by means of different techniques, such as TGA, XRF, CHN elemental analysis, XRD, Mössbauer spectroscopy and cyclic voltammetry. Electrochemical tests were finally performed both in coin cells and by using *in situ* cells: on one hand, coin cells allowed different formulations to be easily tested, on the other *operando* cycling led a deeper insight to insertion process and both chemical and physical changes.

Results of several tests highlighted a non-reversible electrochemical behaviour of the material and a rapid capacity fading over time. Moreover, *operando* techniques report that amorphisation occurs during the discharge.

Acknowledgements

I wish to express my thanks to my supervisor, Professor Marco Giorgetti, for his help, dedication, and trust in me. I thank Professor Lorenzo Stievano as well, for having been my co-supervisor, and for providing me with all the necessary facilities for the research, together with the entire team ICG-AIME at the University of Montpellier.

I am also grateful to all the lecturers I met among these years, for having contributed to my knowledge and my personality. A special thank to Corrado Lugli, a high school teacher, whom I gladly cite for having taught me more about life than about English (not meaning he is a bad teacher).

I take the opportunity to express my gratitude to my martial arts teacher, Mario Venta, for having taught me not just to fight, but above all not to give up in front of difficulties.

I thank my friends, all my colleagues in Bologna and those that I left in Montpellier, for instance Ephrem Terefe Weldekidan and all the other football players.

I finally thank my parents, Shefqet and Mimoza, for having supported me for almost 24 years. The last shall be first.

Contents

List of Figures

List of Tables

Chapter 0

Introduction

0.1 General aspects

A battery is a device that converts chemical into electrical energy.

Batteries have two main functions: first, they act as portable sources of electric power; secondly, they are able to store energy provided by external sources [6].

In order to get a proper voltage or capacity (commonly expressed in mAh), several cells may be connected either in series or in parallel, so that the resulting battery is in fact the sum of different cells [7] [8].

A crucial distinction has to be made between primary and secondary cells: a primary cell converts the energy of a chemical reaction, during which the reactants are consumed in a single discharge process; on the other side, through a current passing in the opposite sense to that of the spontaneous discharge reaction, a secondary cell may be restored. A secondary cell, known as rechargeable cell, could hold less energy and last for a shorter period of time, but it can provide several cycles of discharge/charge, finding a wide market for portable consumer devices. The result is an electrochemical energy storage unit, in which chemical and not electrical energy is stored [6].

Features that a secondary battery should have are (i) the ability to undergo several

Figure 1: Ragone Plot

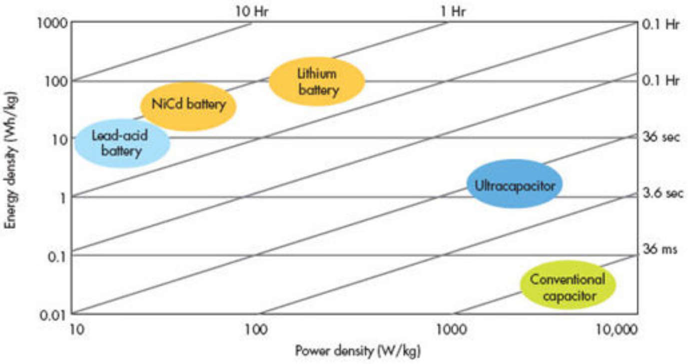

Source: ElectronicDesign.com
November 15, 2007

discharge/charge cycles with high efficiency and reversibility, (ii) a high power/-mass or power/volume ratio in the case of batteries for electric vehicles, where the total vehicle load or even volume matters.

Conventional batteries do not meet the requirements of portable electronic devices, nor those for automotive products, because of their low energy density. For this reason, rechargeable lithium cells have gained higher consideration over the years, providing both volumetric and gravimetric energy density ($\mathrm{E}_0 = -3,04\mathrm{V}$ vs SHE; AW $= 6,941$ g/mol), and displacing nickel-metal hydride (NiMH) and nickel-cadmium secondary batteries in consumer hand-held devices [8].

A way to compare a vast gamma of energy storage devices is the Ragone plot (Figure 1). This bilogarithm chart reports energy density (Wh/kg) on the Y-axis and power density (W/kg) on the X-axis, so that it is possible to read both the energy that a device can deliver and the rapidity of erogation of that energy. Thus, a point (X;Y) on the graph lies on the isocurve characterized by unit slope and erogation time Y/X, that represents the time required for delivering the energy Y at the power X. Actually, energy and power densities are so expressed:

$$Energy\ density \ = \frac{V \cdot I \cdot t}{m} \tag{1}$$

$$Power\ density \ = \frac{V \cdot I}{m} \tag{2}$$

where V is the voltage, I the current, t the time, and m the mass.

As a result, a device that has to last for a long time and is not intended to possess much power density is positioned on the top in the left corner, so that it can supply a great amount of energy. Conversely, applications that need low energy amounts to be activated, but an elevated promptness, lie on the bottom in the right corner. According to this chart, Li-ion batteries have both greater energy and power densities compared to lead-acid and nickel-cadmium batteries, lying on the same isocurve yet.

Lithium secondary cells consist of lithium metal as negative electrode, an active material (AM) as positive electrode, and a non-aqueous lithium-ion containing solution which enables ion transfer between the electrodes: the electrode material should undergo a reversible reaction with lithium ions, i.e. it is reduced during discharge, while oxidized in charge:

$$xLi^{+} + AM(s) + xe^{-} \underset{\text{charge}}{\overset{\text{discharge}}{\rightleftarrows}} Li_{x}AM(s) \tag{3}$$

Active material electrodes may have a porous framework that allows the rapid insertion and extraction of lithium ions with generally little lattice strain.

Otherwise, a different lithium ion source may be adopted, as lithium metal could be either passivated or cause injuries. Li_xAM' can be opted for negative electrode, whereas AM acts as a lithium ion sink, so that Li-ions are intercalated in both electrodes alternatively:

$$Li_{x}AM'(s) + AM(s) \underset{\text{charge}}{\overset{\text{discharge}}{\rightleftarrows}} Li_{x}AM(s) + AM'(s) \tag{4}$$

This strategy is known as *rocking chair philosophy* [6] (Figure 2), and was the first one adopted to overcome the safety hazards related to Li metal anode, as an uneven growth upon Li metal takes place during alternated cycles of discharge/charge (*lithium plating*). Using two insertion hosts rather than one ensures safety, even though a more positive cathode has to be found since the anode has a less negative potential [7].

Commercial *swing* batteries consist of graphitic carbon as negative electrode and

FIGURE 2: Schematic representation of a rocking chair cell

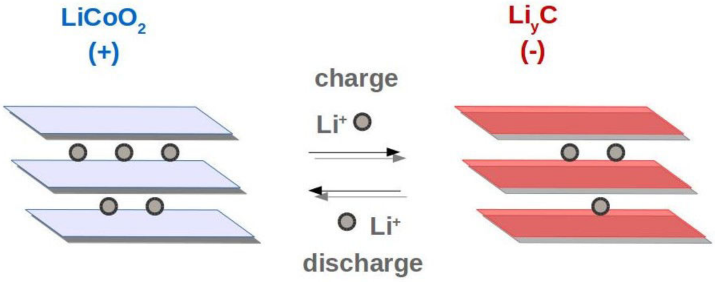

lithium cobalt dioxide as cathode. During discharge lithium is reversibly intercalated in the host material and electrons flow in the external circuit to balance the reaction. During charge the non-aqueous electrolyte mediate the transfer of Li-ions in the opposite direction.

Dealing with electrochemical cells, interfaces play a crucial role. As a matter of fact, the electrode/electrolyte interface may be responsible for a poor cycling, as side reactions may occur. For instance the degradation of the electrolyte is favoured at high voltages (> 4 V versus Li^+/Li) and temperatures, so that high temperature applications are compromised. A strategy to overcome the degradation issue at the active material electrode (cathode) is to encapsulate it either by physical or chemical means. Concerning the anode/electrolyte interface, ethylene carbonate (EC) is usually present as solvent in the Li-ion solution, as it forms an electron insulating yet stable ion-conducting layer on the graphitic anode, which avoids further degradation. This film is called solid electrode interface (SEI) and it is responsible for the stability of Li-ion batteries [7]. On the other side, EC cannot be used alone, as it is solid at room temperature. As a matter of fact, it is commonly mixed with propylene carbonate (PC) and/or dimethyl carbonate (DMC), the former not compatible with graphitic compounds causing exfoliation (if SEI has not been formed yet) [9], the latter melting at 2°C, so not used alone as well in low temperature applications. Mixing EC with other carbonates makes not only the solvent mixture liquid, but optimal viscosity and ion-conductivity are also achieved.

Carbonates are considered optimal solvents for Li-ion batteries, since they are

FIGURE 3: Carbonate solvents

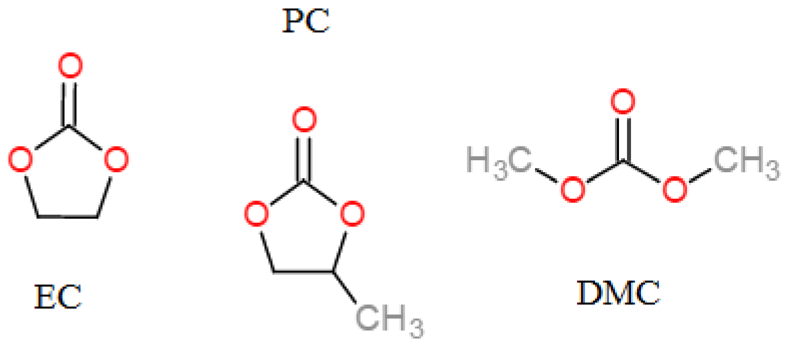

available at an affordable price, and can dissolve Li-salts enough to achieve a good conductivity, although the electrolyte concentration should not overcome the value of 1-2 mol/L for viscosity issues.

In addition, carbonates are preferred to aqueous solvents because of their larger electrochemical stability window. While water degrades below 0 Volts and above 1.2 Volts vs SHE (in conditions of $pH = 0$), carbonates result stable at least in the range $-3 < E < 1.6$ V vs SHE [10].

Nevertheless, a limiting factor could be the electrolyte. Salts of strong acid are used, so that $LiClO_4$, $LiBF_4$, $LiAsF_6$, $LiPF_6$, and CF_3SO_3Li are often present in ion-conducting solutions. Among these, $LiPF_6$ is usually employed for its ionic conductivity, but it is thermally unstable, decomposing in LiF and PF_5 and generating HF if water is present.

$$PF_6^- \leftrightarrows PF_5 + F^- \tag{5}$$

In terms of cyclability, the battery performance would decline. Another option might be lithium imide salts, for instance lithium bis(triflouromethane sulfonyl) imide salt, denoted as LiTFSI, which is safer and more stable than $LiPF_6$.

$LiPF_6$ has a higher conductivity and even a greater viscosity compared to LiTFSI, due to the PF_6^- anion coordination by solvent molecules. However, under the same conditions, the performances result better for LiTFSI than for $LiPF_6$ [11].

Figure 4: FEC reaction

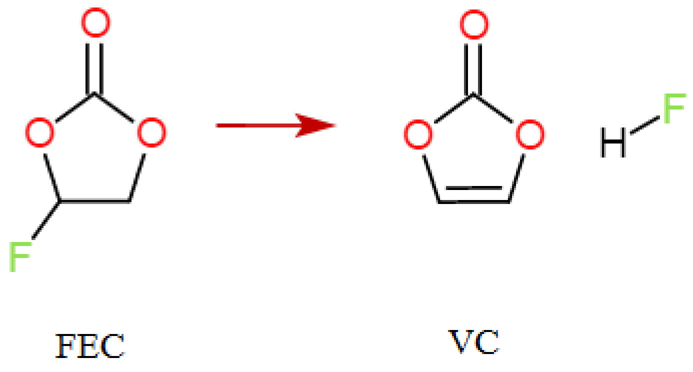

A further option to keep in mind is the possibility of using additives, which enable the usage of unsuitable solvents (SEI-forming additives allow for example PC employment), and enhance long cycle stability. Among these additives, vinylene carbonate (VC) and fluoroethylene carbonate (FEC) are widely used.
VC is a sacrificial additive that is reduced at a higher potential than any present solvent, that is to say it is first-reduced: products that arise from this reduction process are adsorbed on the graphitic anode, helping in the SEI formation and avoiding a structurally porous and highly resistive interfacial layer. The mentioned products derive from an electrochemically induced polymerization through a radical anion, which can be terminated either by a solvent molecule or by another specific additive. Since oxidative polymerization can also occur on the cathode and cause resistance, such sacrificial additives are added in few percentages [12].
FEC does not contain a vinyl functionality, but it can release a HF molecule and generate VC. HF has been reported to have a beneficial effect on the morphology of Li deposition, i.e. limiting the lithium plating [12].

A new appealing choice concerning batteries is the use of sodium instead of lithium as anode, above all for its worldwide abundance. Taking into account the future cost of lithium and the sustainability of the resources, nowadays it is increasingly important to develop new low-cost batteries.
On one hand, Na-ion batteries provide a cheaper alternative to Li-ion batteries, on the other, sodium has a higher mass (AW = 22.9898 g/mol) and a larger ionic

Figure 5: Argon-filled glove box

radius ($r = 1.02$ Å) compared to Li ($r = 0.59$ Å).

Actually, the greater weight and the slighter energy density make Na-ion batteries less competitive than Li-ion ones for mass sensitive applications [13]. Additionally, the reduction potential is less negative ($E_0 = -2.71$ V vs SHE), so that the supplied voltage is reduced.

The actual limiting factors for Na-ion batteries are the low availability of adequate insertion materials (graphitic carbons do not intercalate Na [14]) and the irreversibility of both the insertion and extraction because of side reactions, which are more preponderant than in case of Li-ion batteries [13].

Common electrolytes in Na-ion batteries are sodium bis(trifluoromethane) sulfonimide (NaTFSI), sodium triflate (NaOTf), sodium perchlorate ($NaClO_4$), and sodium hexafluorophosphate ($NaPF_6$), being the latter two the most adopted ones. As Li salts, they are dissolved in solvents characterized by a high permittivity, i.e. ethylene carbonate (EC) and propylene carbonate (PC). Additives are also employed: however, VC does not seem to be an efficient one, contrary to what happens with Li electrolytes. On the other hand, FEC has proved its high efficiency and versatility [14].

Recent studies reveal new cathodic compounds that are able to insert Na-ions and, especially, that could be competitive with Li-ion cathodes in terms of energy density. That is about layered transition-metal oxides, for instance $Na_{2/3}[Fe_{0.5}Mn_{0.5}]O_2$ [14].

However, both Li- and Na-ions batteries require to be assembled or even disassembled inside inert gas-filled chambers (Figure 5). As a matter of fact, both the metals and the electrolyte solutions are air- and moisture-sensitive, and can cause fire hazards. Thus, a new breakthrough might be to adopt aluminium as anode as recently published, in order to achieve at the same time both safety due to the non-flammable solvent, and a high energy density thanks to the trivalent oxidation state of Al [15]. Actually, the theoretical capacity depends directly to the x number of electrons provided per mole of cathode material:

$$Specific\ capacity = \frac{Charge\ stored}{mass} \tag{6}$$

$$Specific\ capacity = \frac{x \cdot N_A \cdot Q_e}{MW} \tag{7}$$

x = number of electrons
N_A = Avogadro's number
Q_e = Charge of an electron (expressed in Coulombs)
MW = Molecular weight of the cathode material
$Specific\ capacity$ expressed in Coulombs/g. but generally expressed in mAh/g.
In this case, the active material AM provides three moles of electrons per inserted mole of aluminium, whereas it supplies just one electron per mole of lithium or sodium. The theoretical capacity associated with the same material would be increased three times if aluminium were adopted instead of a monovalent ion.

$$xAl^{3+} + AM(s) + 3xe^{-} \rightleftarrows Al_xAM(s) \tag{8}$$

One has to keep in mind that even anions may be used: for instance, $Al_xCl_y^-$ could be used in an Al-ion battery, by entering the cathode during charge [15]. Nevertheless, large and multivalent ions can be trapped and block the ion mobility, hence an *ad hoc* host material has to be fine-tuned [16].

In fact, a big issue concerning Al-ion batteries is the cathode material disintegration. As reported, intercalation into natural graphite would involve an enormous expansion of the cathode, that is 50-fold: for sure, such a dilatation would compromise and destroy the structural stability of the material. An alternative to such a problem would be to substitute natural with pyrolytic graphite, which consists of a three-dimensional graphitic foam, distinguished by covalent bonds between graphene sheets. An expansion takes place as well, but the cathode integration is preserved [15].

Other concerns about Al-ion batteries are the the low specific capacity due to low mobility of ions, and the small cell voltage.

All in all, great efforts and progresses have been done, and further works are still in progress, given that rechargeable Al-ion batteries could have a high power density and be safe and low-cost.

0.2 Prussian Blue analogues

A new class of active material electrodes is represented by open-framework structures such as Prussian blue analogues.

Prussian blue, named even ferric ferrocyanide $Fe^{III}[Fe^{II}(CN)_6]$, originally *Berliner blau*, was first and accidentally synthesized in 1704 by Heinrinch Diesbach and had applications not only as blue pigment and replacer of the much more expensive lapis lazuli, but also as antidote. It actually consists of an open-framework structure, which was useful for trapping irreversibly thallium (I) ion, which could replace the interstitial potassium ion deriving from the reactants [17]. This feature, known as ion exchange, is nowadays used for trapping caesium-137 from waste streams in the processing of nuclear fuels [18].

A distinction has to be made between *soluble* and *insoluble* form of Prussian blue, not referring with these terms to real solubility, instead to a tendency to form a colloidal solution or not, due respectively to the absence or presence of vacancies and interstitial cavities [19].

Prussian blue analogues (PBAs) are bimetallic cyanides with a three-dimensional lattice of repeating units of -NC-Fe-CN-M-NC-, where M denotes a transition metal, generally Mn, Co, Ni, Cu, Zn [4]. As iron is commonly present, these compounds are recognised as *hexacyano ferrates*, otherwise in case of absence of iron, they are just called *hexacyano metallates.* Many works have been written about PBAs, for instance regarding electrochemical detection of hydrogen peroxide [20]

FIGURE 6: Structure of a metal hexacyano ferrate

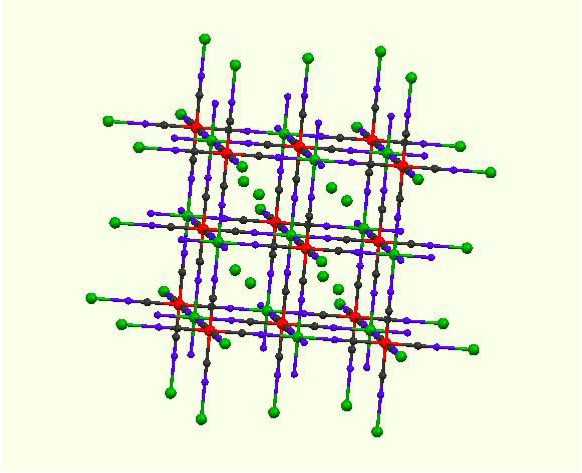

[21].

The cyano ligand acts as a bridge between Fe and M, linking them in a precise fashion, the carbon bound to Fe, while the nitrogen to M (Figure 6). Moreover, iron is usually present as Fe (III) in a low-spin state due to the strong-field ligands, whereas M is a divalent ion. A change in the M oxidation state from (+2) to (+3), compensated meanwhile by interstitial ions, provokes a contraction in the cell dimensions, generally around 10 Å [18]. Both Fe and M can behave as redox centers (verified by means of electrocatalytic properties [22]), so that the resulting capacity may be higher than electrodes with just one metal undergoing a redox reaction.

Through the three-dimensional lattice, Prussian blue analogues are even characterized by flexibility due to the stretching of cyano ligands, which have the function of mediating a metal-to-metal charge transfer as well [23]. As a matter of fact, the C-end is able to remove charge through a π-backbonding, and to place it on the N-end, making possible the interaction between the generally 5Å-distant metals, and giving rise in this way to magnetic and optical properties [24].

A straightforward example of how a bridging ligand may influence magnetic functionalities is given by Tokoro and Ohkoshi: reversible photomagnetism of rubidium manganese hexacyanoferrate $Rb_{0.88}Mn[Fe(CN)_6]_{0.96}$ was investigated. This compound shows a charge-transfer transition from Mn(II) to Fe(III) in the ferromagnetic cubic phase, giving as result the antiferromagnetic tetragonal phase, distinguished by the Jahn-Teller distorted Mn(III) [23].

Another clear example of the role of the cyano ligand derives from Fluck et al., who recorded in 1963 the Mössbauer spectra of both Prussian blue, ferric ferrocyanide, and Turnbull blue, ferrous ferricyanide, and demonstrated they were exactly the same: even though these compounds come from different reagents, an electron transfer from Fe(II) to Fe(III) takes place and the resulting product is the same.

Among PBAs properties, also electrochromism is encountered: $Co[Fe(CN)_6]$ can change its colour by gaining or loosing electrons, being violet in its oxidized state, while green in the reduced form. Furthermore, the colour of cobalt hexacyanoferrate is attributed not only to the oxidation state of Co, but also to its environment: different cations or presence of water alter its aspect [18].

Regarding the porous structure, the open framework is given by repeated vacancies of the octahedral building unit $[M(CN)_6]$. In these cavities both coordinated and weakly bonded water is present, which can be removed below 100°C without modifying the existing structure [24]. Additionally, these compounds can host both Li- and Na-ions due to the large interstices and channels, being so processed for battery use. Even Al-ions have been successfully inserted and extracted as well [16].

Recently, this kind of compounds have gained popularity, not just for their ability to host ions or even small molecules, for instance hydrogen, but also for their convenient price and ease of synthesis.

0.3 Copper ferricyanide and copper nitroprusside

Copper ferricyanide $Cu[Fe(CN)_6]$ is a a Prussian blue analogue where Fe (II) is replaced by Cu(II). Even in this case, two forms are present, one *soluble* and one *insoluble*. The former has a face-centered cubic structure $F\bar{4}3m$, where Fe and Cu ions are octahedrally coordinated to –CN and –NC groups, respectively. The latter has a cubic framework as well ($Pm\bar{3}m$), but 1/4 of the $Fe(CN)_6$ are vacant, with water molecules replacing the empty nitrogen positions in order to complete the coordination sphere of Cu. Thus, Cu atoms are present in this unit cell with three pseudo-square planar coordinated atoms (CuN_4O_2) and one octahedrally coordinated Cu atom (CuN_6), resulting in an average of $CuN_{4.5}O_{1.5}$ [22].

Copper hexacyanoferrate can be easily synthetized through a co-precipitation method: a Cu(II) and a ferricyanide solution are added at the same time under constant stirring, and the product can be collected by filtration. The synthesis takes place at room temperature, it is scalable and relatively cheap.

Many works are available on this compound, due to its surprising electrochemical behaviour when processed for use in battery electrodes. It is actually capable of retaining almost the original capacity after deep discharge cycles at high rates. It is reported that the 75 percent of the initial capacity can be preserved after 40000 cycles at a 17C rate, which means that the battery could perform a huge number of cycles with a high energy efficiency [25].

Copper nitroprusside has a nitrosyl group instead of a cyano ligand. While the cyano group may act as a linking bridge, the nitrosyl one does not. In such a way, the resulting structure has a higher porosity.

Contrary to copper ferricyanide, there may be three redox centers, as not only copper and iron can change their oxidation state, but also nitrogen in the nitrosyl group. Actually, the nitrosyl group is a *non-innocent* ligand and may be present in three different forms within the crystal structure: NO^+, $NO\cdot$, NO^-.

Nitrosyl group could theoretically undergo a redox reaction, changing meanwhile its geometry:

$$NO^+ \xrightarrow{e^-} NO\cdot \xrightarrow{e^-} NO^- \tag{9}$$

$$linear \rightarrow bent \rightarrow bent$$

The resulting battery capacity would be increased due to the number of electroactive species, whereas the geometrical modification could be observed by IR spectroscopy, the linear -NO absorbing around 1940-1950 cm^{-1} [26] [27] [28], the bent form at 1400-1700 cm^{-1}.

The hypothesis of a bending of nitrosyl group may be assisted by the case of sodium nitroprusside $Na_2[Fe(CN)_5(NO)]2H_2O$: according to the published works,

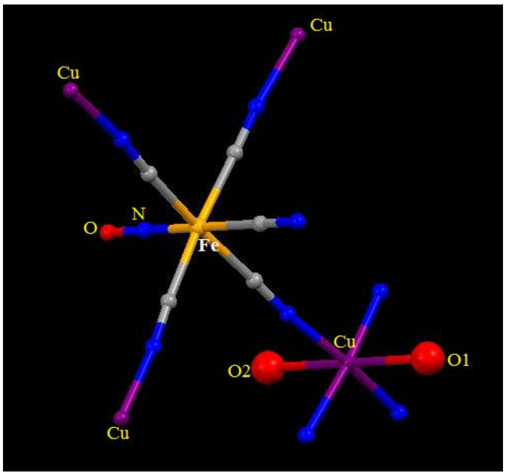

Figure 7: Structure of $Cu[Fe(CN)_5(NO)]\cdot 2H_2O$

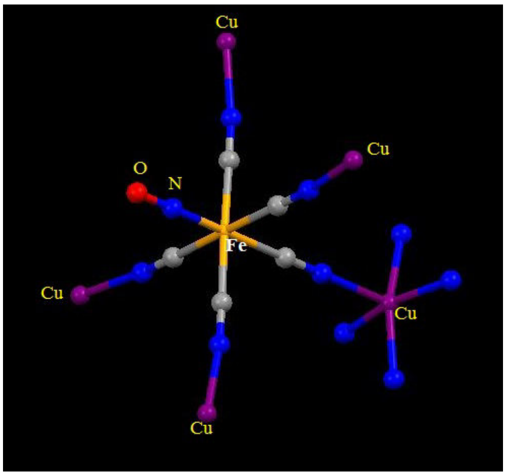

Figure 8: Structure of $Cu[Fe(CN)_5(NO)]$

sodium nitroprusside has been found in two different structures, one having an isonitrosyl, the other one characterized by a bent -NO [29] [30].

In addition, copper nitroprusside could be present either in the hydrated form with two water molecules per unit formula, or anhydrous.

The hydrated structure is orthorhombic with space group $Amm2$ and $Z = 2$. The iron coordinates to five cyanide ligands and one nitrosyl, the copper is surrounded by four equatorial cyanides and two axial water molecules. The axial -NO and -CN groups do not act as bridge ligands. Moreover, copper shows axial elongation according to bond lengths calculations due to its d^9 electronic configuration and Jahn-Teller distortion (Figure 7).

The anhydrous structure is tetragonal with space group $Imm4$ and $Z = 2$. Copper looses two coordination positions while water is eliminated: for this reason the structure changes and copper coordinates not only to four equatorial cyanides, but also to an axial one, so that the coordination sphere resembles to an elongated pyramid of square base [31] (Figure 8).

In the anhydrous structure the distance between the oxygen-end of nitrosyl and copper ion is reported to be 2.93 Å [31]: according to the model of hard spheres, this spacing corresponds to the Van der Waals interaction distance, the oxygen radius being 1,52 Å and the copper one 1,40 Å. This interspace suggests no chemical bond between oxygen and copper, and therefore that the nitrosyl group does not bridge the two metals. However, the atoms are close enough to allow a polarization of the -NO electron cloud by the copper ion, which results in an increase of the NO π-backdonation towards iron [31].

Copper nitroprusside has been processed as electrochemical sensor [32]; on the contrary, nothing is reported in literature about its use as cathode. As the study of this material could be chemically interesting and may have a technological application for a large-scale energy grid, the present work is based on it.

Chapter 1

Synthesis

The synthesis of copper nitroprusside was based on a co-precipitation method from 20 mM solutions of $CuSO_4 5H_2O$ (Code 209198) and $Na_2[Fe(CN)_5(NO)]2H_2O$ (Code 71778), used as purchased by Sigma Aldrich [33]. The simultaneous addition took place in 90" at 40°C under constant stirring, stopped after 60". A green solid precipitate occurred almost instantaneously (Figure 1.1). The green colour results from a charge transfer, which is absent in sodium nitroprusside (dark purple/ almost black) [26]. The solution was aged for two days, then the precipitate was collected by centrifugation. First, the supernatant was removed: each test tube contained about 5 mL of solution, and was centrifugated at 4000 rpm for 5 minutes.

FIGURE 1.1: Synthesis batch

Table 1.1: Yields

Batch	Yield %
1	71.4
2	71.4
3	69.3

Afterwards a washing with distilled water was repeated three times (4000 rpm for 6 minutes). The precipitate was vacuum dried at 60°C overnight and placed in a desiccator. After a week, a part of the solid was treated at 130°C for 6 hours. The synthesis was performed three times.

Six samples resulted in this way: AM1, AM2, AM3 from each batch, and AM1T, AM2T, AM3T treated at 130°C.

The yield was calculated *a posteriori* according to the real composition. From table 1.1 we can conclude that the synthesis was quite reproducible in terms of yields.

Chapter 2

Experimental part

2.1 TG Analysis

Thermogravimetric analysis was performed in air from 25°C to 500°C with a heating rate of 5°C/min, and rapid cooling.

Samples showed approximatively the same thermogram, in particular the main mass loss takes place at the same temperature, suggesting a high similarity between them. Moreover, there is a mass loss at low temperatures (60-100°C) just for two samples (AM2, AM3), implying evident presence of water.

However, samples are considered *anhydrous*, or better *non hydrated*, since for being hydrated the related mass loss would have been higher than 10%. In this case, water is doubtless present, but it should be in the interstices, and not in any coordination position.

Figure 2.1 reports the superimposed curves of all the samples, subtracted to the reference one (empty holder) and normalized to the initial sample mass. The major weight decrease starts roughly at 240°C, while it finishes at 270°C, being the maximum loss rate at 255°C.

According to mass losses and subsequent composition analysis, the samples may loose globally three cyano groups and one nitrosyl above water molecules, as reported in literature [31]. However, a slight loss is generally displayed at 160°C,

Figure 2.1: TG Analysis

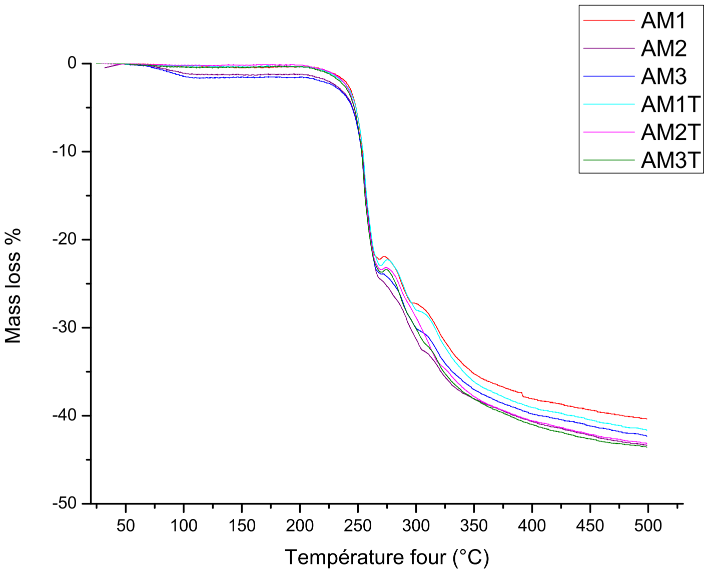

whereas the synthesized compound results stable up to 240°C.

Another TGA was carried out to verify the hygroscopy of the material: a representative has been exposed to air for two weeks, and then analysed. No difference has been reported respectively to the sample stocked under inert atmosphere.

Lastly, the diffractograms of the final powders were recorded and showed iron and copper oxides, as expected.

An unexpected point is that thermograms are more or less the same. After the synthesis a part of the sample was vacuum dried at 130°C, while the other part was vacuum dried just at 60°C. We expected an orthorhombic structure for the samples dried at 60°C, and a loss of two water molecules per unit formula, i.e. roughly a 10-12% mass loss, whereas a tetragonal phase for the samples dried at 130°C, and no great amount of water within the structure. As also further revealed by XRD, samples are all tetragonal, which is in agreement with mass losses diagrams.

This could mean that the procedure after the synthesis, in particular the vacuum-drying at 60°C, provoked the dehydration process and the structure modification of the compound.

2.2 XRF

XRF was performed by means of a PANalytical Axios$^{\mathrm{mAX}}$ Spectrometer on pellets using boric acid as filler and with a concentration of the synthesized material of roughly 26%. From XRF spectra Fe/Cu ratio and C/N ratio were calculated (Table 2.1), while the presence of both sodium and sulphur (contained in the precursors) was not detectable, even though it is commonly reported in literature the presence of sodium in the lattice interstices.

No clear-cut difference can be appreciated between the samples. As a matter of fact, spectra are superimposable.

TABLE 2.1: Atomic ratios from XRF

Sample	Cu/Fe ratio	N/C ratio
AM1	0.63	1.15
AM2	0.63	1.17
AM3	0.69	1.15
AM1T	0.66	1.05
AM2T	0.66	1.17
AM3T	0.68	1.18

2.3 CHN Analysis

CHN analysis gave information on carbon, hydrogen (i.e. water) and nitrogen content. Each sample has been analysed three times and the mean values were adopted as the real ones.

Table 2.2 reports the ratios normalized to the nitrosyl group. As XRF, samples from different batches are similar; besides, the temperature-treated samples differ from the non-treated ones just for the water content.

The generalized chemical formula for the synthesised compound could be calculated: $Cu_{0.8}[Fe_{1.2}(CN)_5(NO)]xH_2O$, x being far lower than 2, and corresponding to the last column of the relative table.

Table 2.2: Ratios from CHN

Sample	N/C	Fe/NO	Cu/NO	H2O/NO
AM1	1.21	1.20	0.75	0.47
AM2	1.21	1.22	0.77	0.51
AM3	1.20	1.19	0.81	0.56
AM1T	1.22	1.15	0.76	0.32
AM2T	1.20	1.25	0.83	0.32
AM3T	1.23	1.09	0.74	0.24

2.4 XRD

XRD was performed on a X'pert PANalytical diffractometer in the 2θ range $10 \leq 2\theta \leq 70$ ° using Cu K-alpha ($\lambda = 1.5418$ Å).

Diffractograms were recorded for the six samples twice: once as they were after the synthesis procedure using a standard sample holder, the second time after vacuum-drying in Büchi at 100°C overnight using a kapton protective film, by assembling the holder in a glove-box. The profiles were refined using the program FULLPROF and a Pseudo-Voigt peak shape.

Powders are crystalline and patterns correspond to anhydrous $Cu[Fe(CN)_5(NO)]$ [28] [31], as expected from the thermograms. After a profile matching with constant scale factor, the space group results $I4mm$, while cell parameters a and c have been optimized from the reference ones, appearing 10.06 Å and 10.92 Å respectively for all samples (Figure 2.2).

Thus, the drying does not affect the structure of the sample.

2.5 Mössbauer spectroscopy

Mössbauer spectroscopy can easily reveal the oxidation state of iron. In this case, a doublet is obtained, suggesting a divalent and not a trivalent ion (Figure 2.3). For this reason, assuming as (+2) the oxidation state of copper, the nitrosyl ligand in the structure should be in the form of -NO^+ in order to achieve electro neutrality. The Mössbauer parameters fairly agree with literature: $QS = 1.83(1)$ mm/s; $IS = -0.28(1)$ mm/s; $LW = 0.30(1)$ mm/s, being QS, IS and LW respectively

Figure 2.2: Diffractogram of copper nitroprusside

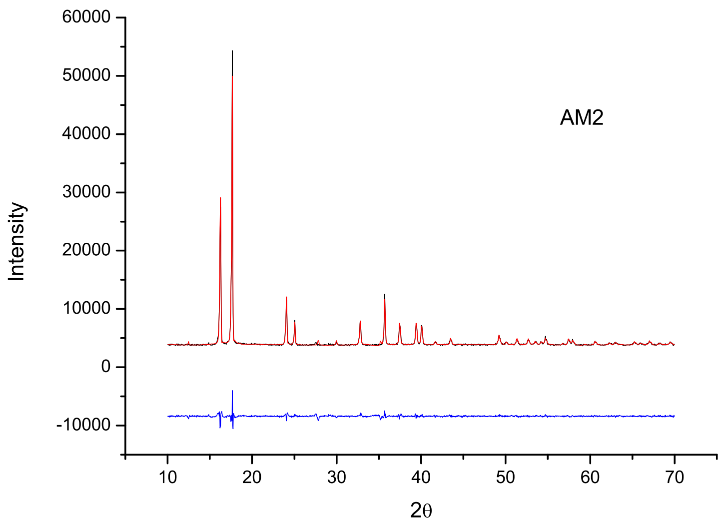

Figure 2.3: Mössbauer spectrum

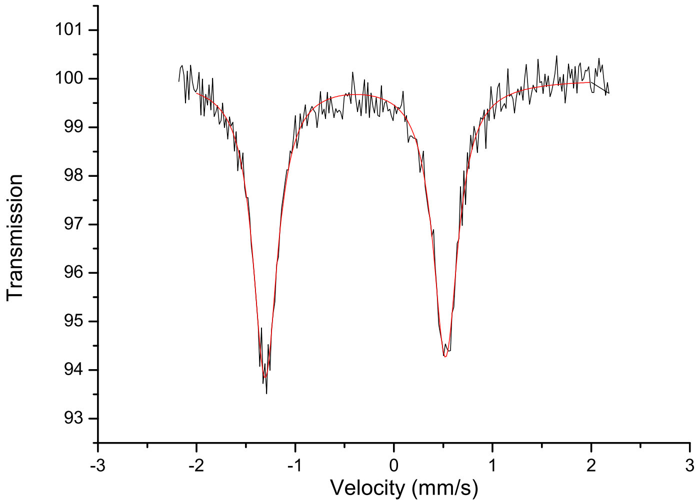

the quadrupole splitting, the isomeric shift and the line width, in accordance with literature [31].

Furthermore, the peaks' asymmetry reflects the anisotropy that characterizes the material. The peaks have the same width, but different intensities due to the Goldanskii-Karyagin effect, commonly present in anisotropic crystals.

2.6 CV technique

Cyclic voltammetry is useful to detect the redox reactions and the potential at which they occur.

For a cyclic voltammetric analysis an electrode paste was used. This paste contained 75% of active material, 20% of carbon black, and 5% of PTFE. A standard three electrode Swagelok® cell was used, adopting lithium metal foil both for counter electrode (anode) and reference. The scanning rate was set at 0.01 mV/s, while the potential window spaced from 2.0 V to 3.5 V, relatively to the reference. During reduction three different reactions take place, respectively at 2.64 V, 2.69 V and 2.82 V. After having approached the lowest potential value and having let the oxidation start, no evident oxidation process can be detected, and among cycles even the reduction does not appear any more. A slight oxidation can be identified in a broad potential range, i.e. between 2.4 Volts and 2.9 Volts (Figure 2.4).

All in all, not only the first reduction is irreversible, but also the electrochemical behaviour of the material changes, given that it cannot repeat itself one more time. In order to make a comparison between copper nitroprusside and the precursor, sodium nitroprusside, a cyclic voltammetry was even performed on the latter. Besides, before attempting to cycle the product, it would not be a waste of time to test the reagent.

A CV was done under the same conditions, by changing just the active material compound.

A higher reversibility character has been noticed, even though the first cycle differed from the next ones.

During the first cycle, clear reductions take place at 2.21 and 2.57 Volts, while oxidations are evident at 2.59 and 2.81 Volts. Second and third cycles are similar between them and have different redox potentials from the first one: reductions are weakly present at 2.44 and 2.59 Volts, a further one more intense at 2.21 Volts. Oxidations occur at 2.57 and 2.76 Volts (Figure 2.5). However, 3rd cycle does not clearly show reduction at 2.59 Volts and oxidation at 2.76 Volts (Figures 2.6 2.7).

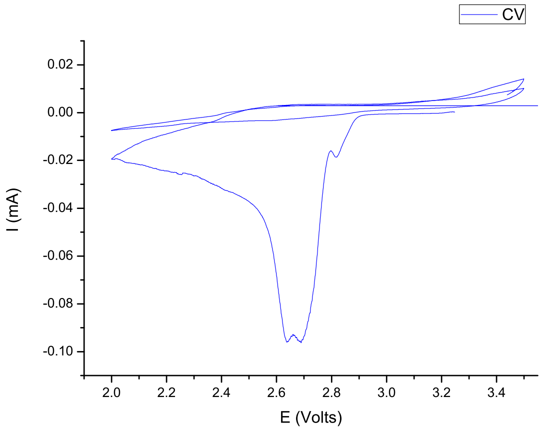

FIGURE 2.4: Cyclic voltammogram of copper nitroprusside

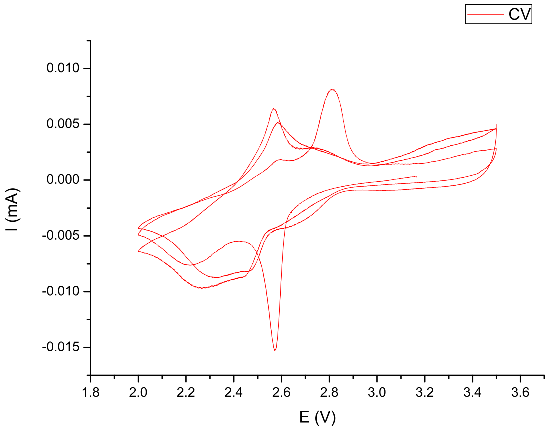

FIGURE 2.5: Cyclic voltammogram of sodium nitroprusside

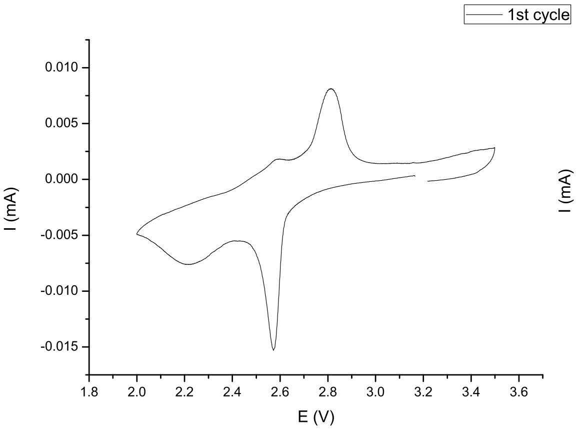

FIGURE 2.6: Cyclic voltammogram of sodium nitroprusside. First cycle

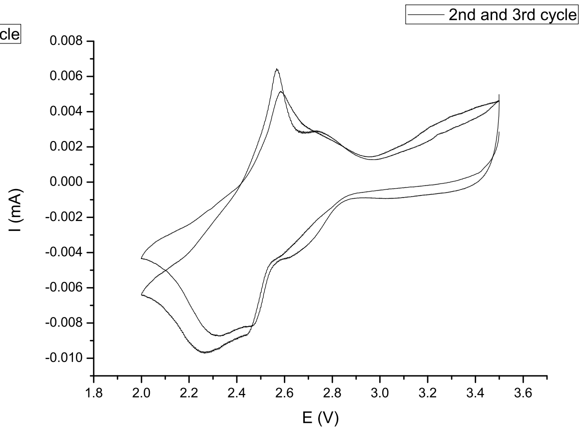

FIGURE 2.7: Cyclic voltammogram of sodium nitroprusside. Second and third cycle

For its reversible behaviour, sodium nitroprusside may be cycled.

Relatively to copper nitroprusside and taking into account the electrode masses, sodium nitroprussise presents a lower redox activity, as the variation of current intensity is smaller. In other words, related specific capacity is supposed to be roughly ten-times smaller than for copper nitroprusside, by considering that molecular weights do not differ much.

Chapter 3

Results and Discussion

EC-Lab$^{®}$ Software provided GCPL (Galvanostatic Cycling with Potential Limitation) technique, dedicated to battery testing. A current is imposed and therefore the battery cycles under galvanostatic mode. A potential window can be set in order to limit the potential decrease during discharge (reduction) and increase during charge (oxidation).

An open circuit mode is available as well.

Tests could be done either in coin cells or in swageloks. Coin cells (Figure 3.1) were used for their availability and ease to work with. Their geometry is quite simple, as they consist in stacked layers: two cases enclose the electrodes, separated by the electrolyte solution. After having been stacked, coin cells are closed by means of a mechanical machine.

Besides, *in situ* cells were useful to test the batteries under cycling, helping in finding out informations about the chemical changes that happen. The cells are geometrically different, as their purpose is different. Indeed, coin cells' aim is just to test electrochemically a given material, whilst an *in situ* cell has a further objective, that is to observe how that material undergoes to chemical and physical modifications during the test by spectroscopic means. Actually, *in situ* cells have at least one transparent window, depending on the chosen spectroscopic technique. XRD *in situ* cells have two beryllium windows, transparent to X-rays, Mössbauer cells have two Be windows as well but the cell geometry is different, for they work

FIGURE 3.1: Coin cell geometry

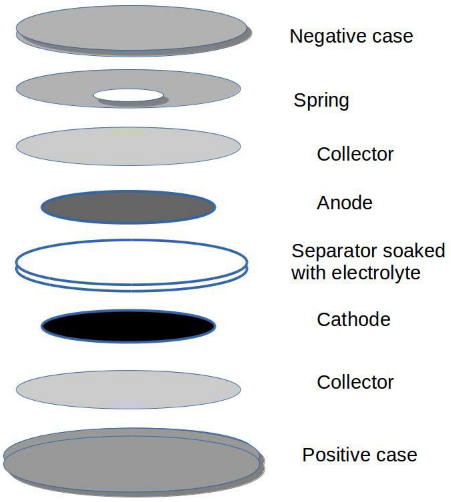

in transmission mode, while IR cells possess a diamond window.

In situ measurements could be done both at room temperature and at a different temperature, unfolding various operating conditions.

Plus, a measurement with an *in situ* cell could be done in two different modes: *in situ* or *operando*. The first way refers to a measurement done by pausing the battery and by recording the spectrum shortly after it. Instead, the second manner refers to a measurement done without pausing the battery. Both modes have their cons, since recording a signal after having stopped a battery could allow the material to relax, while if the battery does not halt, the spectrum regards a span of time over which the material changes, even if the difference could be neglected.

Speaking of electrochemical performances, they could vary based on the electrode thickness and electrode mass. For this reason, it is crucial to test cells with different mass loads. Moreover, even changing the percentage of the electrode constituents may help in getting cycling improvements. For instance, a higher conductivity may be achieved by increasing the carbon content.

A further factor that plays an important role is the current rate, i.e. the imposed current. It is generally calculated from the theoretical capacity, dividing it by a chosen factor. Let's take an example: if one mole of Li per mole of AM should enter the structure in 20 h, the theoretical capacity (in mAh) should be divided by 20 h to get the current (mA) that allows the desired insertion rate. In this

Figure 3.2: Specific capacity vs C/rate

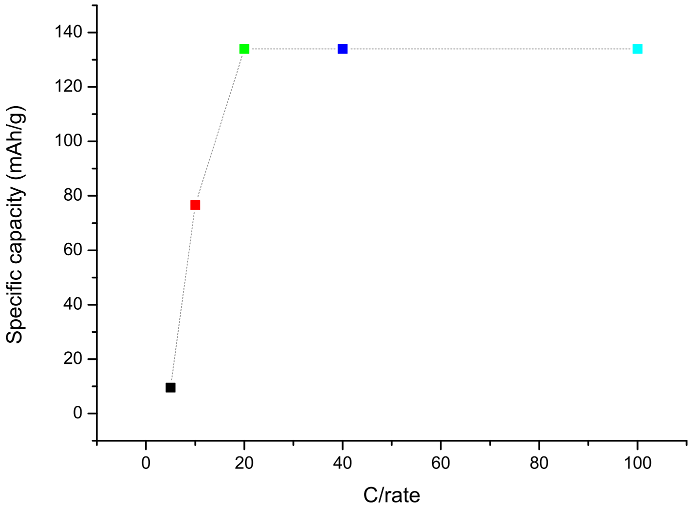

case, the current rate is denoted as C/20, a typical rate value. A current rate of C/40 would be twice slower, while 5C would insert 5 moles of Li per mole of AM in just one hour.

A material that can be cycled both at low and high currents with little capacity fade is an excellent material. Commonly, at high current rates the capacity is lower and the battery is able to insert and extract less ions, as proven by some made tests.

Graph 3.2 was obtained for different PTFE-based electrodes made of copper nitroprusside, under the same conditions of potential window and electrolyte solution ($2 < E < 3.5$ Volts, $LiPF_6$ in EC:PC:3DMC without additives), by changing meanwhile the current rate (C/5, C/10, C/20, C/40, C/100). As shown here, if the insertion takes place in a longer time, the specific capacity increases up to a certain value, above which the capacity is maximum and remains constant. From 10 mAh/g at C/5 rate, it rises up to 134 mAh/g if C/20 rate is employed.

In this case, a C/20 rate seems a fair compromise between analysis elapsing time and obtained capacity.

3.1 Coin cell tests

3.1.1 PTFE-based electrodes

Electrochemical tests were performed first on PTFE-based electrodes, containing 75% of active material (cathode), 20% of carbon black, and 5% of PTFE. The constituents were mixed in an agate mortar, so that thin films were obtained and properly cut (Figure 3.3). Lithium metal foil was adopted as anode, LiPF6 1M in EC:PC:3DMC without additives as electrolyte.

FIGURE 3.3: PTFE electrode. From powder to coin cells

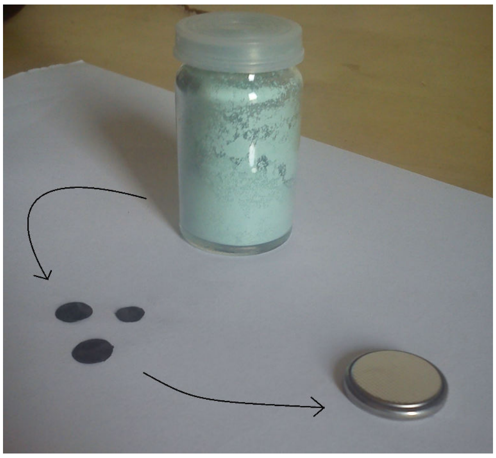

Before testing copper nitroprusside, some tests were done on sodium nitroprusside. A good reversibility is displayed among the cycles, even though the specific capacity results quite poor. Actually, just 0.1 Li moles are inserted in 1 mole of cathodic material during reduction, and vice-versa it is extracted in oxidation (Figure 3.4).

It is even important to underline that to obtain such a result, different tests were done at different current rates, and that if the battery is let cycling at a rate higher than C/40, it does not run well. As a matter of fact, the shown cycles have been recorded at a C/40 rate.

Despite the reversible electrochemical behaviour, sodium nitroprusside has a too low capacity, even for a secondary battery employment. Even more so, it is interesting to move to copper nitroprusside.

Figure 3.4: Cycling on sodium nitroprusside

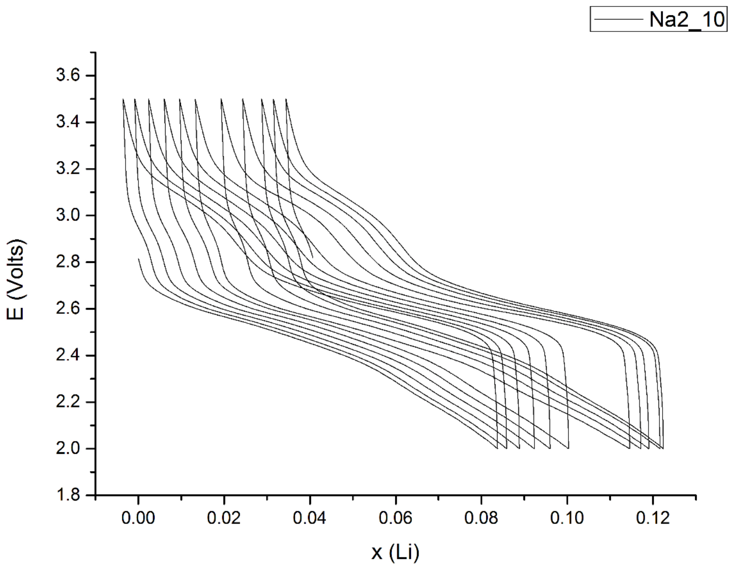

First tests on copper nitroprusside were done in a wide potential window, i.e. between 1.5 V and 4.5 V vs Li^+/Li. When nothing about the reference is reported, it is generally referred to the redox couple Li^+/Li, or in case of Na-ion batteries to the couple Na^+/Na.

The first two cells were assembled with a load of active material respectively of 20 mg/cm^2 and 10 mg/cm^2, with a C/20 rate (Figures 3.5). The electrochemical curves (EC) report the potential as a function of x Li inserted or extracted per mole of cathodic active material, which is proportional to the specific capacity. The cells have initially an open circuit voltage of approximatively 3 Volts and, given that there should have been no ion (sodium in the case) to extract, they were first discharged (a negative current was applied and lithium insertion was enabled), and then charged through a positive current to allow Li extraction.

According to the curves, no clear reproducibility was reached by varying the mass load (different x values are approached during reduction), nor a good cycling performance attained, since the battery does not properly work even in the second cycle of discharge. Anyway, the cell with the higher mass load was able to insert a larger amount of equivalents, which is surprisingly high relatively to other similar compounds, e.g. copper hexacyanoferrate. Copper ferricyanide can actually insert just one mole of lithium-ion per mole of active material at about 4 Volts vs Li.

Figure 3.5: Electrochemical curve. First tests on copper nitroprusside

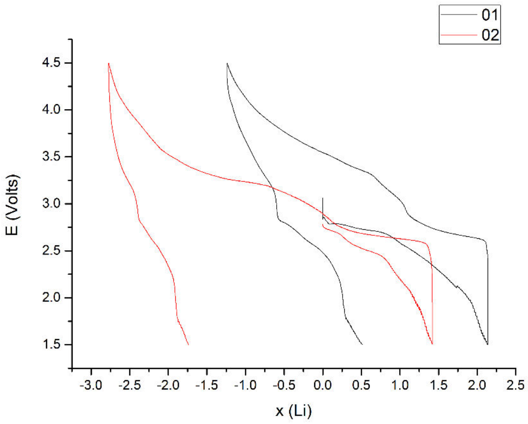

Figure 3.6: Electrochemical curve. Third test on copper nitroprusside

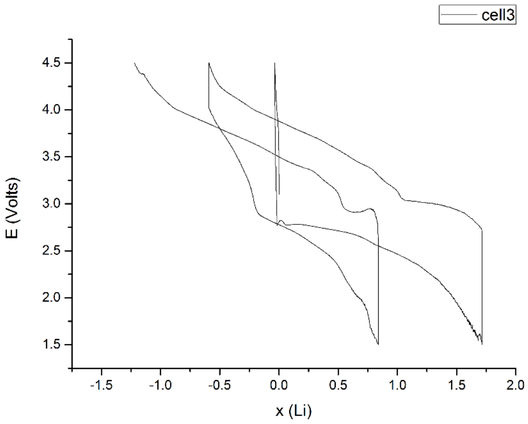

Another striking point is that negative x values are reached during oxidation: it might mean that an over-extraction has taken place, but in fact there should be no other ion over the inserted lithium. As proven by XRF, no sodium is present within the structure.

The third cell, with an active material load of 33 mg/cm^2, was first charged and then discharged (Figure 3.6). During the first charge process, no ion can be extracted, as expected. Consequently, side reactions occur.

Afterwards, it behaves like the previous cells, approaching negative x values. It might mean that something in the first discharge completely changes the electrochemical behaviour of the material. However, a slight improvement in the cycling performance could be noticed, given that the curve is more reversible, but on the contrary a higher capacity is achieved with the first cell.

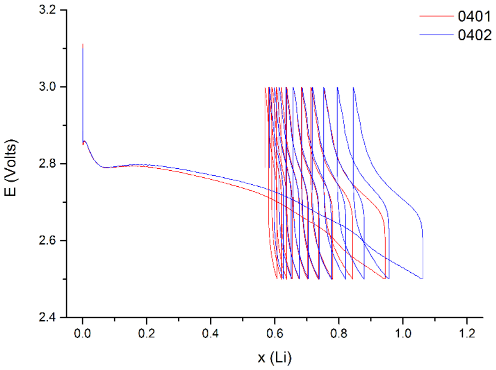

Figure 3.7: Electrochemical curve. Potential window: $2.3 < E < 3$ Volts

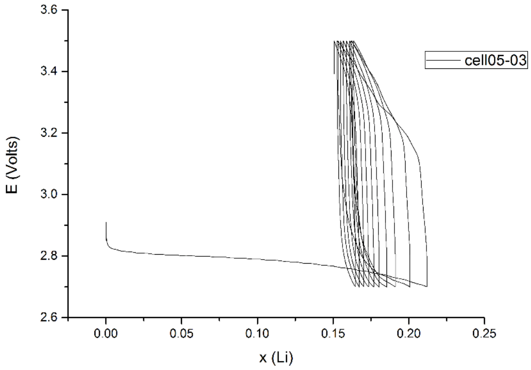

Figure 3.8: Electrochemical curve. Potential window: $2.7 < E < 3$ Volts

According to the cyclic voltammogram it seems that reduction takes place between 2.6 and 2.8 Volts, while oxidation in a wider range, from 2.4 to 2.9 Volts. The potential window was subsequently reduced, first to $2.3 < E < 3$ Volts (Figure 3.7),and secondly to $2.7 < E < 3.5$ Volts (Figure 3.8).Despite the tuned potential window, no satisfactory reversibility could be obtained, even by stopping the reduction so early. As a matter of fact, for the reported curves, the capacity fades too rapidly over the cycles, and the ability of the material to host Li-ions rapidly decays till total incapability.

It has therefore been decided to widen the window: lower potentials permit a larger insertion, while greater oxidation potentials a larger extraction. Actually, it has been noticed that a strong polarization is present, since a greater potential has to be applied to extract the inserted ions, even stopping at the very first plateau. So increasing the upper limit could be convenient to take out more lithium. The selected window spaced from 2 Volts to 3.5 Volts.

Different tests were done in order to verify reproducibility: several PTFE-based electrodes were so prepared. While keeping the parameters constant, it has been noticed that the electrochemical curves referred to the first discharge appear quite similar, especially in the first part, up to the very first plateau (Figure 3.9). Therefore, a quite good reproducibility is obtained among different electrodes just up to few inserted Li-ions, while the same could not be said for the rest of the curve. Further works could be done in order to improve the electrode reproducibility.

Figure 3.9: Discharge comparison

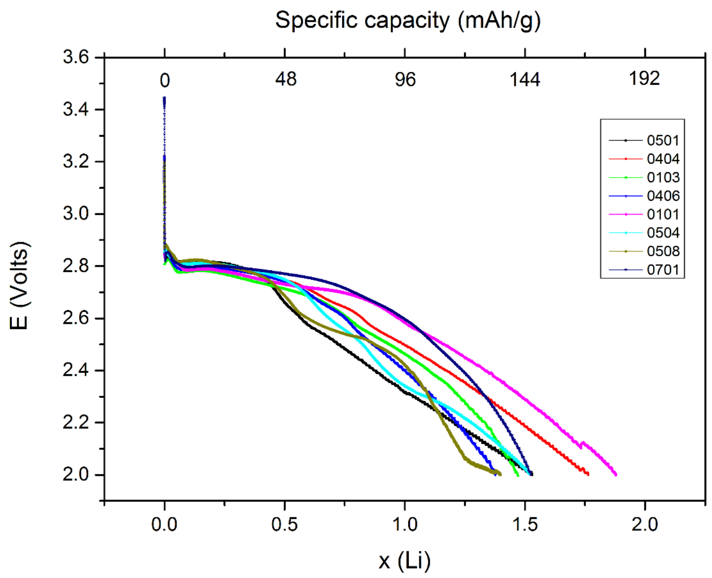

Figure 3.10: Cycles of discharge/charge

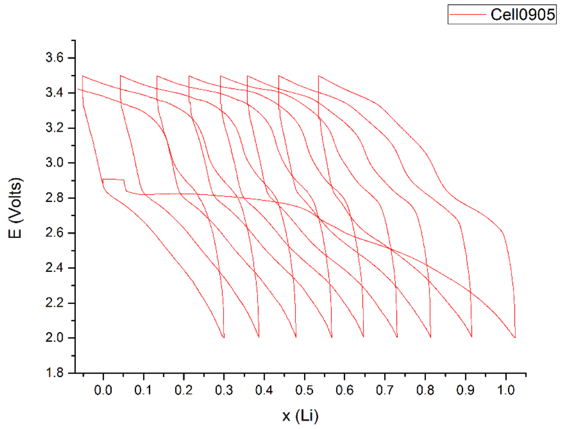

An ordinary example of an electrochemical curve is reported in figure 3.10. Several cycles are reported, where discharge and charge take place alternatively. Each cycle terminates by a relaxation time of 2 hours, not visible in the graph.
The curve tends to move left, towards smaller values of x, while capacity constantly fades as usual (Figure 3.11). Like other experiments, the insertion-extraction window (labelled Δx) decreases among the cycles (Figure 3.12), leading to the end of the battery in few cycles.

Different solvents and electrolytes were adopted in order to improve the cyclability. In particular, (i) $LiPF_6$ was used with additives (Figure 3.13), (ii) LiTFSI

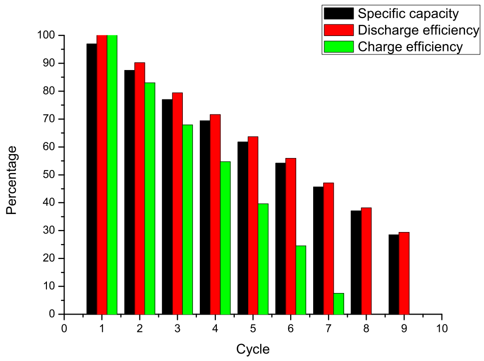

FIGURE 3.11: Specific capacity and efficiency as functions of cycle number

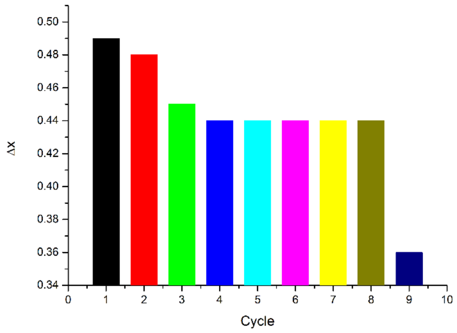

FIGURE 3.12: Δx variation among cycles. $LiPF_6$ electrolyte's case

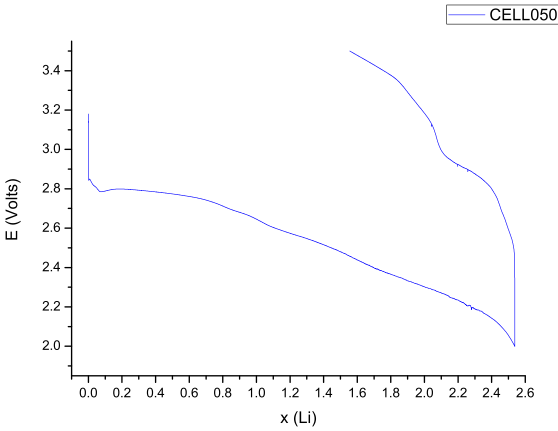

FIGURE 3.13: Electrochemical curve with $LiPF_6$ in EC:PC:3DMC, 1% VC 5% FEC

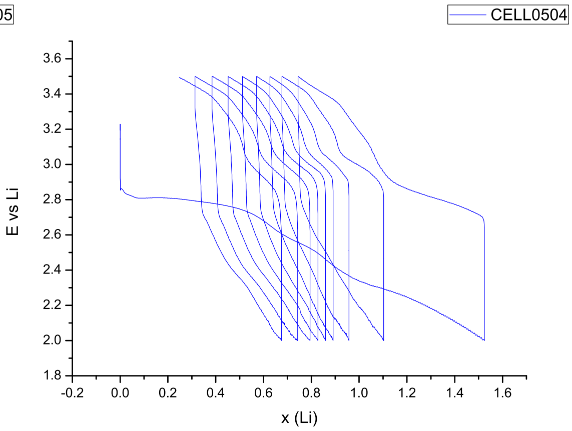

FIGURE 3.14: Electrochemical curve with LiTFSI in EC:PC:3DMC

replaced $LiPF_6$ while keeping constant the solvent mixture (Figure 3.14).

Additives may remarkably reduce side reactions in different ways, e.g. by preventing solvent degradation. For this reason, 1% VC and 5% FEC were added to the employed electrolyte solution ($LiPF_6$ in EC:PC:3DMC), and electrochemical tests were done under the same previous conditions.

The curve shape 3.13, both in discharge and charge, appeared the same as preceding tests, i.e. with the same insertion/extraction potentials. However, the most striking point was that the insertion was significantly greater, and more than 2 moles of lithium-ions could be introduced. In the same way, Li could be removed more than usual (around $1x$ Li-ions was extracted), even though the percent amount of extracted ions relative to the inserted value emerged to be lower.

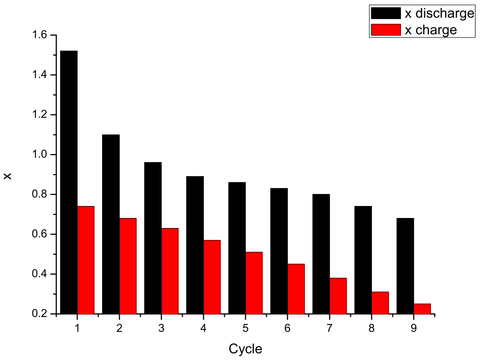

FIGURE 3.15: Capacity fading over time. LiTFSI electrolyte's case.

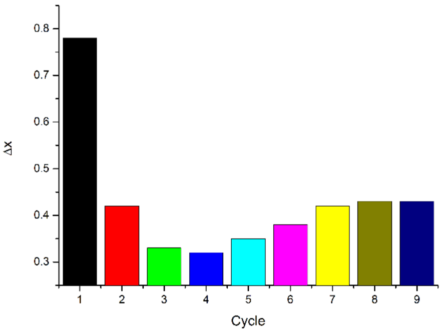

FIGURE 3.16: Δx variation among cycles. LiTFSI electrolyte's case

Differently, LiTFSI is recognized to be more stable than $LiPF_6$, so that side reactions are limited and at the same time the battery life may be prolonged.
The first cycle appeared quite efficient 3.14, as ions put and taken away were also this time higher than usual, though lower than in case of additives.
Half of the extraction took place in a limited potential window, between 2.7 and 2.8 Volts, so that half of the charge occurred almost at constant potential.
Despite this, capacity rapidly faded and further cycles encountered a deep loss of efficiency (Figures 3.15 3.16).

3.1.2 Slurry-based electrodes

Another way to prepare an electrode consists by making a slurry: weighted amounts of cathodic material (AM), carbon black (CB), carbon nanofibers as optional, and a binder are first homogenized in an agate mortar, then put together in a ball mixing jar with few ceramic balls (four are enough). By adding an appropriate solvent and mixing the content of the jar for one hour at least, the slurry is ready to be taken off the jar and be spread on a support of either Cu or Al, depending on the operating potential window.
The only way to know how much solvent is needed is by trial and error, until when an adequate viscosity is found after having mixed the inner content of the jar: too dense slurries may have some little lumps of material and consequently

Table 3.1: PVDF-based electrode. First composition.

Composition	Amount
AM	200 mg
CB	40.0 mg
PVDF	26.6 mg
NMP	1000 μL

an inhomogeneous dispersion, whose active material concentration is not after all well-known, while too diluted slurries are not well-suited to be spread on a support.

The prepared slurry has to be spread by a blade of reported height: different blades are available, depending on the optimal mass per unit surface that each electrode should approximatively have. A typical height value is 150 μm.

After the accurate spreading, the supported electrode area has to be carefully dried either in air or in oven, so that the entire solvent can evaporate and leave the coating.

In many cases, the adopted binder is polyvinylidene fluoride (PVDF) and N-methyl-2-pyrrolidone (NMP) the solvent.

The two most interesting features of a slurry-preparation are (i) the possibility of preparing several electrodes at the same time, (ii) the homogeneity of the film spread on the support, that means a reproducibility among the electrodes. Actually, PTFE-based electrodes could be not identical, as the thinning part could be problematic: if active material powder sticks on the mortar, or if the mixing and thinning have not been done for enough time, a non-homogeneous concentration of the material may arise, determining different compositions along the surface. On the other hand, PTFE-based electrodes may require a small amount of material for the electrode preparation: for example, using 10 mg of active material, it is possible to get five electrodes with a small diameter (4 mm).

First tests were done on a 75% AM, 15% CB, 10% PVDF electrode composition (Table 3.1), using an Al foil instead of a Cu one, even if both metals could have been used for the working potentials. This composition resulted to be too diluted and not easily spreadable.

Further tests were so done with 80% of AM, 10% of CB and 10% of PVDF, with

TABLE 3.2: PVDF-based electrode. Second composition.

Composition	Amount
AM	200 mg
CB	40.0 mg
PVDF	26.6 mg
NMP	750 μL

FIGURE 3.17: Cycling on a slurry-electrode

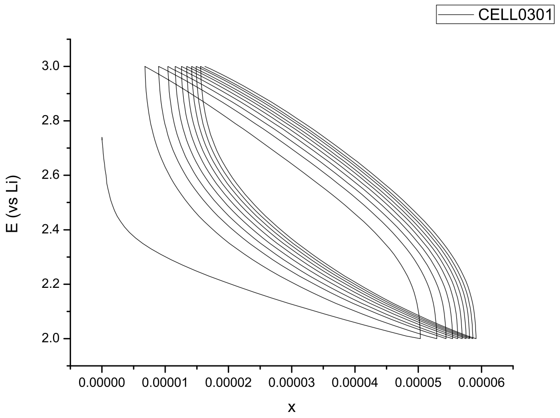

less solvent (Table 3.2): This electrode composition resulted to have acceptable physical properties.

First of all, the coating was dried in air for four days, then cut with a diameter of 12 mm, and further dried in Büchi (vacuum-dried) at 70°C overnight.

Electrochemical tests were done in the potential range $2.0 < E < 3.5$ V at a C/10 and C/20 rate, with Li-metal foil as anode and $LiPF_6$ in EC:PC:3DMC as electrolyte. The mass load of active material was relatively quite high for slurry electrodes, that is ca. 4 mg/cm^2.

The most surprising occurrence is the total inability of the electrode to insert any Li-ion, whatever the applied current rate (Figure 3.17). To investigate the reason why no cycle was obtained at all, an *ex situ* XRD was recorded on the electrode before cycling, and compared with the active material pattern. (Figure 3.18).

For PVDF-electrode, the comparison clearly revealed the change of the original structure, whose pattern almost disappeared, while new peaks appeared. In particular, a very intense peak came into view. Database matching reported metallic iron as the most favourite compound. The unambiguous explanation still misses,

FIGURE 3.18: Pattern comparison between PTFE- and PVDF-based electrodes

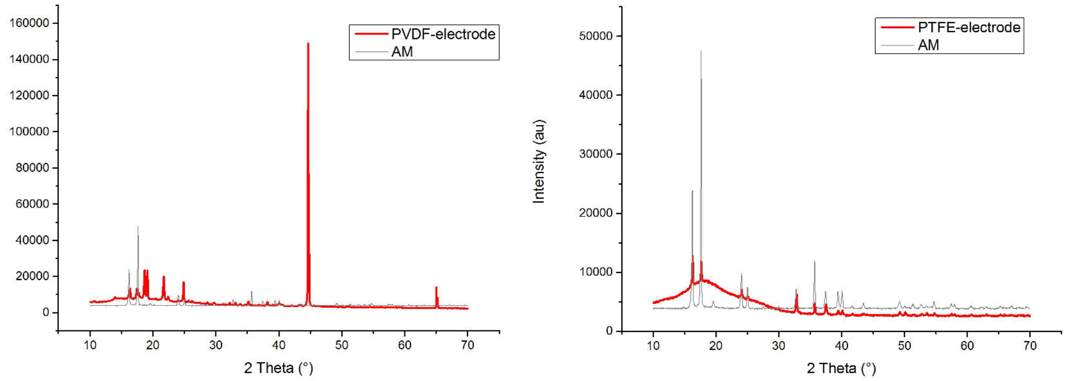

but it could be that the solvent (NMP) was responsible of the structure modification.

For PTFE-electrode instead, the pattern did not change, but just a lowering in intensities and increasing of background have been displayed, for amorphous material has been added.

The next step was to try another solvent, and to prepare a water-based electrode. Carboxymethyl cellulose (CMC) is usually used in combination with water.

Carbon nanofibers were added in this round. Purchased vapor grown carbon fiber (VGCF) has excellent thermal and electrical conductivity, strength property and slidability (lubricity), and can be easily dispersed as well.

Electrode slurry with 70% AM, 9% CB, 9% VGCF-H (distinguished by a high apparent density), 12% CMC, was prepared. 1100 μL of water were used.

The coating was not spread with a blade, but simply with a spatula, in order to achieve a high mass load. The drying was exploited in oven at 60°C, and then in air.

The resulting electrode film had such a composition to allow the separation from the supporting metal foil: in other words, the film was auto-supported.

The active material mass load resulted to be roughly 8 mg/cm^2.

Electrochemical cells were done on coin cells, at C/20 rate (Figure 3.20) as well as at C/10 (Figure 3.19). LiPF$_6$ in EC:PC:3DMC without additives was used as electrolyte solution.

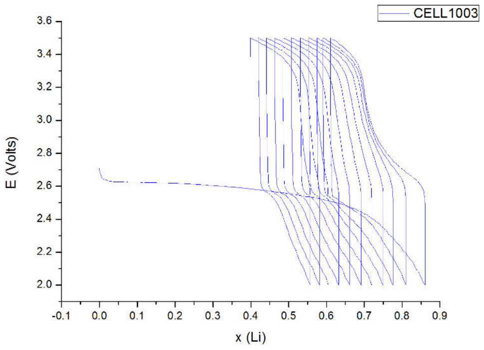

FIGURE 3.19: Electrochemical curve. CMC-based electrode at a C/10 rate

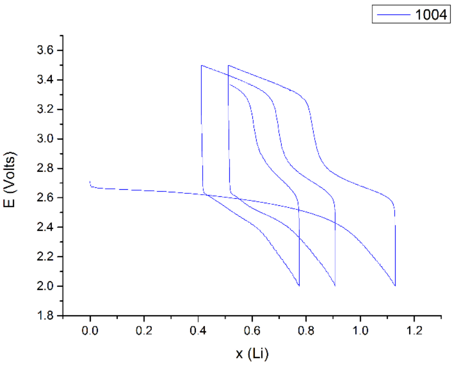

FIGURE 3.20: Electrochemical curve. CMC-based electrode at a C/20 rate

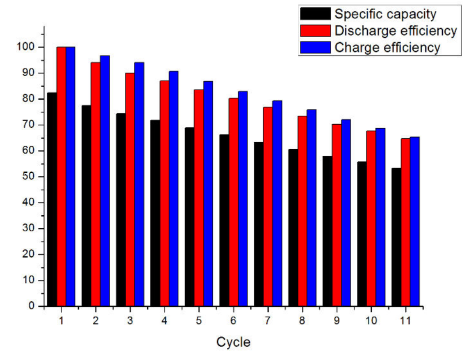

FIGURE 3.21: Electrochemical curve. Capacity fading of a CMC-based electrode

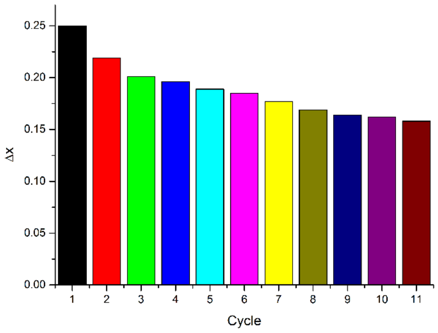

FIGURE 3.22: Electrochemical curve. Δx variation of a CMC-based electrode

The electrochemical curve appeared quite different from the one deriving from PTFE-based electrodes: there were not distinguishable insertion potentials, Li-insertion occurred in one single step, and foremost the material seemed to cycle well both at C/10 and C/20, demonstrating under this aspect to work better with CMC than with PTFE. Furthermore, for the C/10 cycled electrode, the specific capacity was a bit lower than in the case of PTFE-based electrodes, fair enough yet. The capacity fading is constant and slow compared to PTFE-formulation, and performances appear quite stable among cycles (Figure 3.21 3.22). The absolute amount of inserted and extracted ions is lower, yet.

It has been noted that CMC-formulation works better in case of a *conversion* process of insertion. Generically, the reversibility of a secondary cell may lie in a reversible interchange between the original state A and a second state B which is formed during the intercalation, or between two amorphous states C and D, physically and chemically different from the starting one. Such a reversibility condition is typical of *conversion* processes.

As proved by *operando* XRD, amorphisation takes rapidly place during discharge, even in the very first moments, and steadily intensifies among reduction time. Accordingly, the studied insertion process might be of a *conversion* type.

3.1.3 Na-ion batteries

As previously discussed, Na-ion batteries have made inroads into research, as they could be an attractive option to Li-ion batteries. For this reason, tests with a Na-metal foil on the investigated material have been evaluated and here reported. PTFE-based electrodes were tested under different conditions, using different solvent mixtures, electrolytes and current rates.

The first group of tests was done using $NaClO_4$ as electrolyte in PC. Various C/rate were tried, but it has been noted that relatively better performances were got with slow current rates.

As represented in figure 3.23, at a C/20 rate the sodium insertion took place in different steps, as highlighted by noticeable insertion potentials. The extraction, instead, was obstructed and did not occur significantly. It seemed in this way that sodium insertion was more irreversible than lithium one. Speaking of cyclability it is on these terms irrelevant.

Other tests were done using $NaPF_6$ in bis(2-methoxyethyl)ether (DEGDME) at a C/50 rate (Figure 3.24). By changing the solvent mixture, even the electrochemical curve changed: actually, a single potential insertion is present, and this is surprisingly almost constant. Such characteristic turns out to be important in battery applications, as a constant discharge (and eventually charge) potential makes the battery erogate a constant voltage while working. On the other side, the extraction results really poor, though better than the previous case.

Lastly, copper nitroprusside was tested at C/50 with $NaPF_6$ in another solvent,

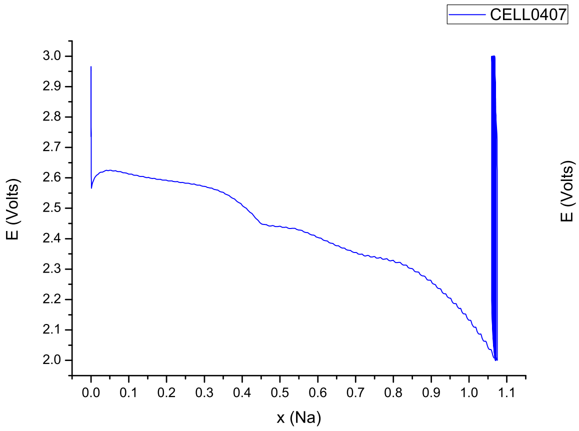

FIGURE 3.23: Na-ion battery. Electrolyte solution: $NaClO_4$ in PC

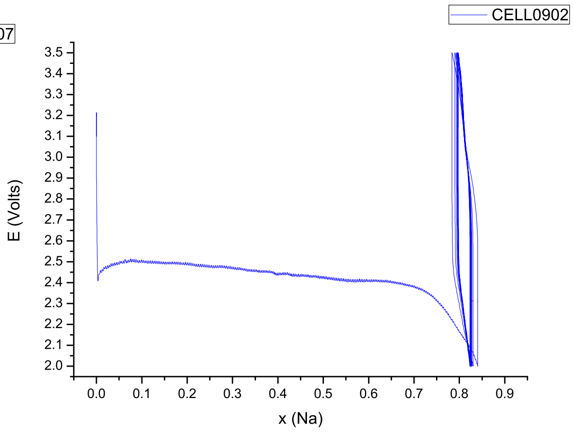

FIGURE 3.24: Na-ion battery. Electrolyte solution: $NaPF_6$ in DEGDME

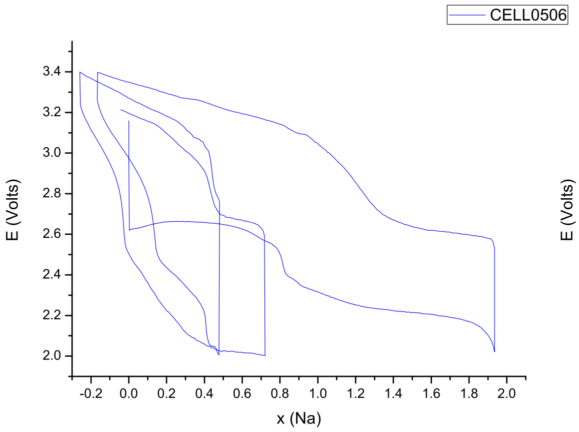

FIGURE 3.25: Na-ion battery. Electrolyte solution: $NaPF_6$ in EC:DMC

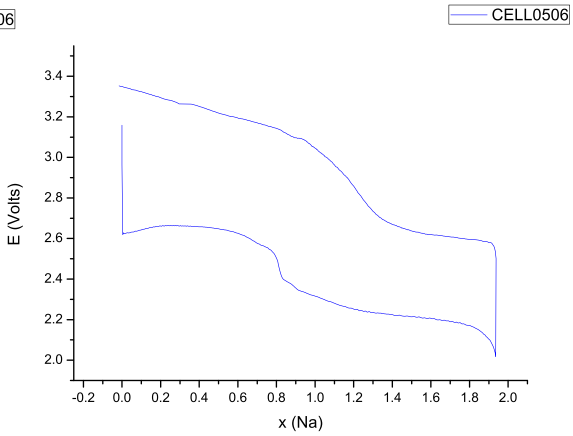

FIGURE 3.26: Na-ion battery. Electrolyte solution: $NaPF_6$ in EC:DMC. First cycle

composed this time by equal parts of EC and DMC. For the first and distinct time, an extraction was feasible.

Both the entire cycling (Figure 3.25) and the first cycle (Figure 3.26) are shown. From the first cycle it is quite surprising how the material could extract all the Na-ions inserted, with a polarization included between 0.4 and 0.6 Volts. As a matter of fact, it seems that the ions inserted at 2.6 Volts are removed around 3.2 Volts, while those inserted at 2.2 Volts are roughly extracted at 2.6 Volts.

After the first cycle, the capacity considerably fades, even if it appears that the third cycle experiences an improvement, since more than 0.7 Na are inserted and a charging plateau is present at 2.6 Volts.

Better performances are obtained in the last case using $NaPF_6$ in EC:DMC. This could be due not only to the electrolyte, but also to the solvent mixture: probably, viscosity and ion-mobility play an important role in determining performances and cyclability.

3.2 *Operando* techniques

Operando techniques are useful to make assumptions about the insertion mechanism.

Different types of *in situ* cells are used, depending on the spectroscopic technique. Before introducing *operando* tests' results, it would be useful explaining how an *in situ* cell is assembled. Although *in situ* cells geometry varies from different kinds of experiment, similarities are enough to dedicate a brief part to it.

3.2.1 Geometry of an *in situ* cell [1]

An *in situ* cell needs some requirements, such as the ease of assembling and disassembling, which is done in an Ar-filled glove box, the ease of cleaning, the opportunity of several uses, a good isolation from air after having closed it, the ease of connection to the potentiostat, and a good electrical contact between the electrodes.

An *in situ* cell (Figure 3.27) is first of all constituted by two parts, the main body and the plunger. The body is directly in contact with the positive electrode (cathode), while the plunger is in contact with the anode. The main body is fasten at one side to the top part of the cell, while at the other side is screwed together with the plunger.

The top part of the cell has an outer diameter of 50 mm and an inner one of 20

FIGURE 3.27: *In situ* cell

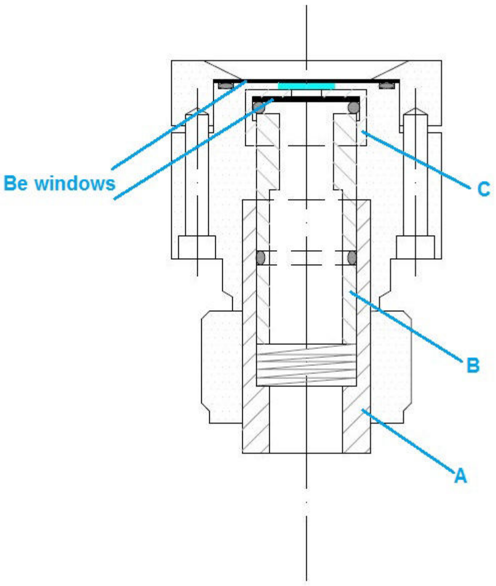

mm, with an hole of 40 mm. Inside this hole is placed a Be window of $\phi = 40$ mm. To guarantee hermeticity, the top part is fixed with six stainless steel screws to the main body, after having put an o-ring between the Be window and the body. The cathodic material is laid on the Be window. An aluminium foil is added between them if a potential higher than 3.5/3.8 Volts is used, in order to avoid Be oxidation. On the positive electrode is put the separator soaked with the electrolyte solution, whereas the other side of the separator is in contact with the anode, i.e. the Li-metal foil.

The negative electrode is generally sticked to the piston. The plunger ($\phi = 20$ mm) is made of three parts: A, B, C. A is connected to B thanks an o-ring and a spring, whereas B is screwed to C, where another Be window is placed. On this Be window, the Li-metal foil is sticked, simply by applying a pressure.

After having fixed and stacked all the components, the main body (+) and the plunger (-) are screwed together: to avoid short circuit, the inner part of the body is covered by a Mylar thin film, so that a direct contact is hindered.

As the cell has to be assembled by hand, it is necessary to push enough the plunger, otherwise a good electrical contact is not established. Non worn-out gaskets and a relatively strong spring may be helpful.

3.2.2 *Operando* XRD

As host materials are able to insert ions in their channels and cavities, a general peak shifting in XRD diffractogramms would be expected. The intercalation would make the interplanar distance increase, so that a gradual peak shifting could be highlighted towards greater 2θ angles.

Among research works, it is even common to find out that a given phase may be modified by ion-insertion, and new phases arise from the original one. This fact could be proved by emerging patterns during the electrochemical test.

One could say in this way not only that new phases appear, but even if the process is reversible or not. As a matter of fact, by letting the battery cycle over several steps of discharge and charge alternatively, it is feasible to record different diffractogramms corresponding to different grades of reduction or oxidation, that is intercalation or de-intercalation respectively. In other words, it would be possible to follow the electrochemical process by peak shifting. In case of a reversible process, peaks swing from the original position to another one.

Operando XRD was performed on a Empyrean Diffractometer using a Cu Kα radiation in the 2θ range $10 < 2\theta < 47$ °, in order to avoid some irrelevant peaks, e.g. those of beryllium. A deep discharge was carried out on a PTFE-based electrode, down to 0 Volts, at a C/20 rate, adopting Li-metal as anode and $LiPF_6$ in EC:PC:3DMC without additives as electrolyte solution (Figure 3.28). Each diffractogramm was recorded in a span of approximatively 60 minutes.

On the investigated material, *operando* XRD revealed no peak shifting, that means no change in structural parameters: thus, it might seem that the Li insertion was not carried out by intercalation in the porous framework. However, very large channels may not be influenced by small ions between the planes, even if a slight increase in cell parameter could be expected yet. Actually, even for other open-framework structures with large channels, a little shift is usually present.

Moreover, amorphisation might occur over time, since peaks' intensities decreased during the Li-insertion, while background rose up. For sure a long-range order gradually vanished, as well as a short-range one, demonstrated by *operando* XAFS.

FIGURE 3.28: Electrochemical curve during *Operando* XRD

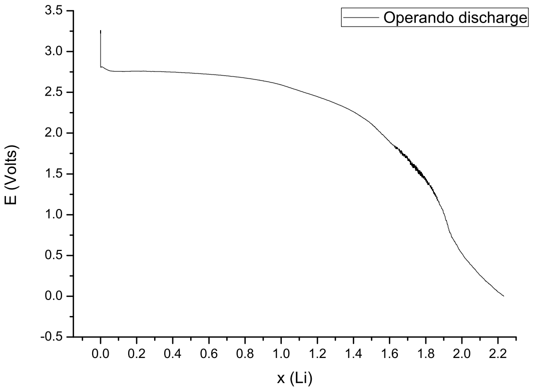

Figure 3.29 reports some of the patterns recorded during the discharge: diffractograms corresponding to different Li-insertion amounts (labelled as x) are superimposed. Figure 3.30 reports a comparison between two diffractograms, one recorded before cycling, the second after 20 hours of discharge (corresponding to one inserted Li at a C/20 rate). Figure 3.31 shows instead a comparison with the pattern recorded after 40 hours, i.e. after two inserted Li. Among time, background signal increases, while peak's intensities decrease.

A very important aspect of the registered diffractograms is the presence of two new peaks, at 23.3° and 33.2°. A matching with database structures was done, by considering not only possible phases deriving from the cathodic material and lithium-ions, but also those that might arise from an interaction with the solvent and the electrolyte. However, no reliable compound has been found to match with the reported peaks.

The most plausible compound could have been iron (III) fluoride FeF_3, as its peaks perfectly match with the appeared ones, both for peaks position and relative intensities, also considering the fact that fluoride ion may originate from electrolyte degradation.

Nevertheless, this is not sufficient to assert that FeF_3 is formed during the electrochemical test: Mössbauer spectroscopy revealed for the starting material just the presence of iron (II), and *operando* XRD was performed just for the discharge down to 0 Volts, that means just for the reduction. Iron (II) is not able to become iron (III) under the conditions of a negative applied current. Consequently, iron

FIGURE 3.29: *Operando* XRD. Patterns collection

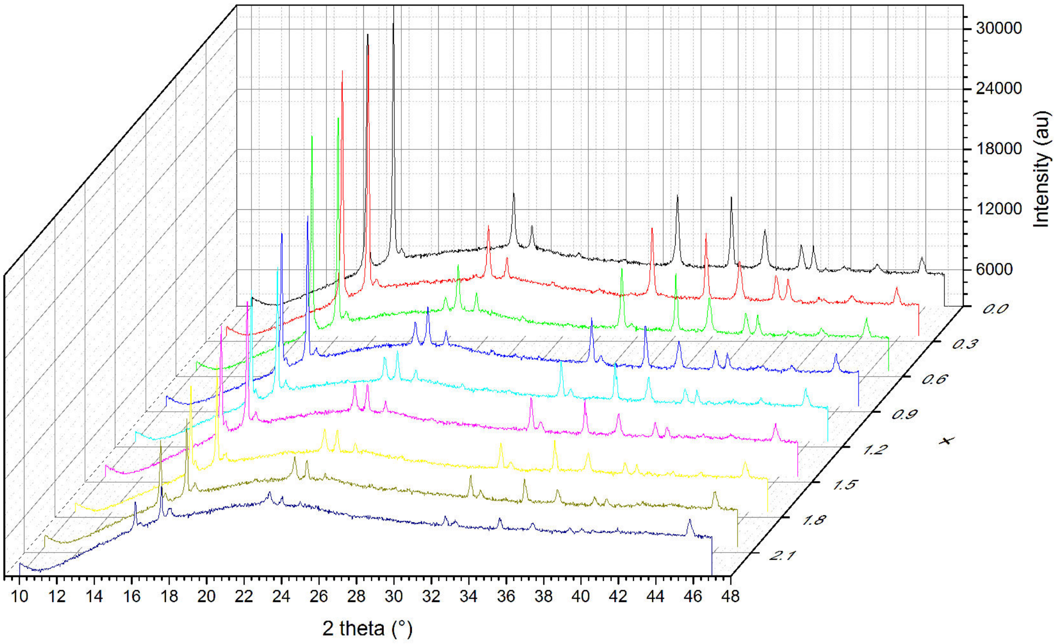

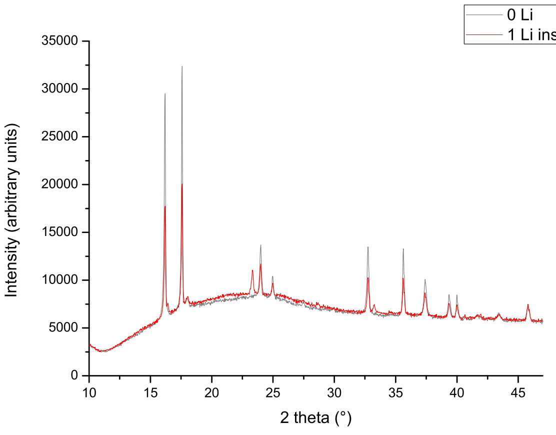

FIGURE 3.30: XRD comparison after 20 hours

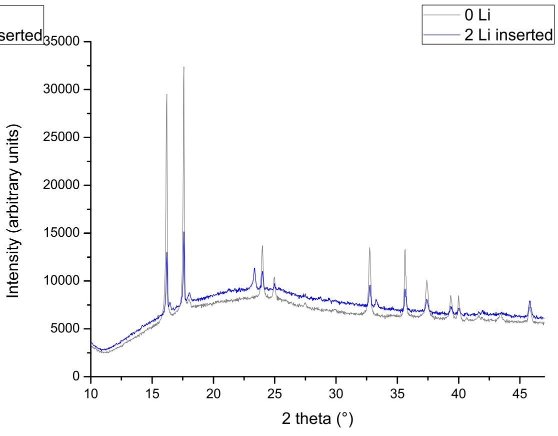

FIGURE 3.31: XRD comparison after 40 hours

(III) fluoride was discarted as possible phase for chemically-inherent reasons.

3.2.3 *Operando* Mössbauer

Mössbauer *in situ* cells are quite similar to XRD *in situ* ones. The difference between them concerns essentially the plunger. While XRD works in diffraction, so that X-rays are reflected on the surface, Mössbauer works in transmission. Therefore, it is necessary that the incoming radiation would be able to enter the cell, so that in a Mössbauer arrangement the plunger is hollow and ends with another beryllium window.

Operando Mössbauer was carried out in the $2 < E < 3.5$ V potential window, at a C/20 rate, adopting Li-metal as anode, $LiPF_6$ in EC:PC:3DMC without additives as electrolyte solution, and a PTFE-based electrode as cathode. Spectra were recorded in a transmission mode each four hours.

Mössbauer spectra revealed no participation of iron to the discharge, as expected: iron (II) could not be reduced further under these conditions. Instead, iron (II) might be oxidized during charge to iron (III), but no data is available about it. Actually, the charge did not properly work (Figure 3.32), and the spectra measured after the end of discharge gave no clue about its participation to the redox. In fact, a big issue concerning *in situ* cells is a non-efficient electrical contact, due to its geometry. Undesired outcomes are non-working discharge and/or charge processes.

Despite this, other information could be extracted from the spectra during discharge. A gradual signal decreasing took place, as transmission grew up (Figure 3.33). No clear interpretation has been found out yet, even if such a fact may be the result of dissolution of iron. Accordingly, the compound may be dissolved in the electrolyte solution, causing an intensity lowering in absorption of γ rays. Furthermore, this decreasing does not take place from the beginning, so that this change occur throughout a second moment in the discharge.

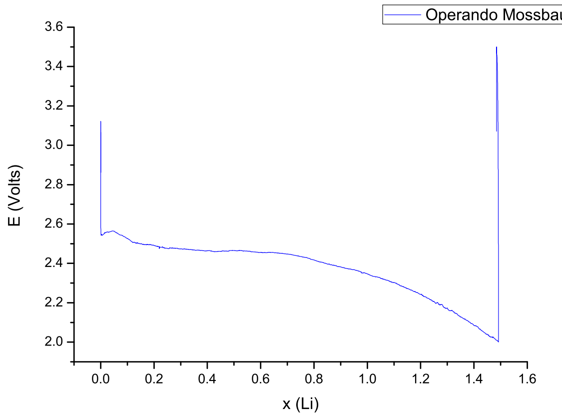

FIGURE 3.32: Electrochemical curve. *Operando* Mössbauer

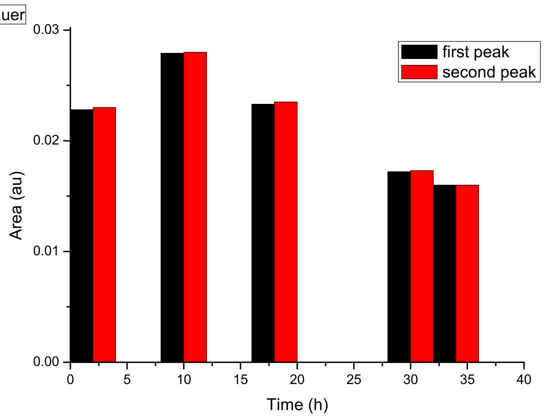

FIGURE 3.33: Mössbauer signal decreasing over time

3.2.4 *Operando* IR

IR *in situ* cells are the same as XRD *in situ* ones. Just the transparent window is made of diamond ($\phi = 2$ mm) instead of Be.

Electrochemical test was done under the same conditions of the other *operando* cells: PTFE-based electrodes as cathode, Li-metal foil as anode, $LiPF_6$ in EC:PC:3DMC with 1% VC and 5%FEC as electrolyte solution, cycling between 2 and 3.5 Volts, at a C/20 rate (Figure 3.13).

ATR FT-IR spectra were recorded each three minutes from 400 to 4000 cm^{-1}.

In literature is reported that the linear -NO stretching is around 1940 cm^{-1}, while not so much is told about the bent form regarding inorganic compounds: some data are available for organic compounds, which report the stretching of bent -NO between 1400 and 1700 cm^{-1}.

In the IR spectra, the position of the stretching of the linear -NO has been first evaluated: in accordance with literature, the relative band has been found at 1940 cm^{-1} before the electrochemical test. Moreover, three bands are expected for the cyano ligands, due to geometry and symmetry, but just two are present at 2157 and 2207 cm^{-1}.

Afterwards, a comparison has been done between the original spectrum and the spectra recorded during discharge and charge.

In the discharge, it has been noticed that three bands disappear, respectively at

FIGURE 3.34: *Operando* IR. Comparison between initial and reduced state

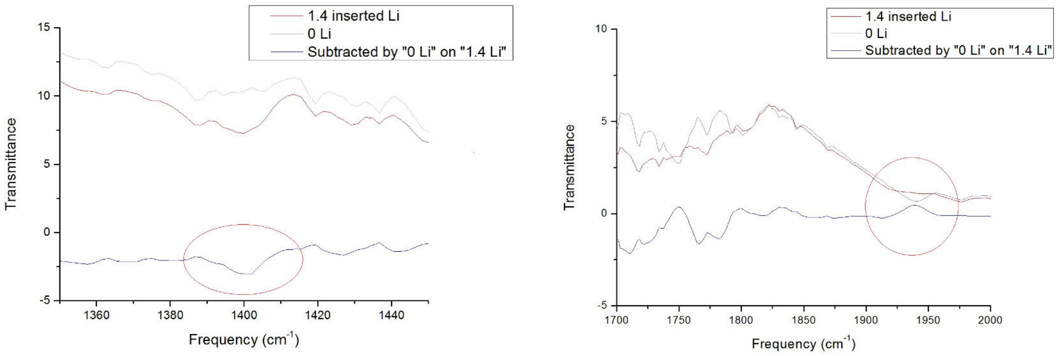

1750, 1940 (linear NO), and 2207 cm^{-1}, while another band appears at 1400 cm^{-1} (Figure 3.34). Other changes occurs at low frequencies, such as intensity increase or decrease of signals, or bands shift.

The fact that the band corresponding to the linear form of -NO disappears and another one at 1400 cm^{-1} becomes evident might be the result of the reduction of nitrosyl ligand. A certain interpretation is not available, but this could be a likely understanding of the process.

If this interpretation were true, it would mean that nitrosyl group participates to the redox. Just metals with at least two reversible oxidation states usually take part to such electrochemical processes, so the possible contribution of a ligand may open various attractive alternatives to batteries progress and innovation.

Even a signal corresponding to cyano ligands (2207 cm^{-1}) is lost, and this may signify that a change in geometry occurred, that is in agreement with *operando* XRD and EXAFS.

During oxidation, no return to the initial state is observed (Figure 3.35). Actually, all formed or lost bands are kept as they were in the discharge. This result is in fair agreement with the cyclic voltammogramm, which shows neither a clear oxidation process, nor a reversible behaviour among cycles.

FIGURE 3.35: *Operando* IR. Comparison between initial and oxidized state

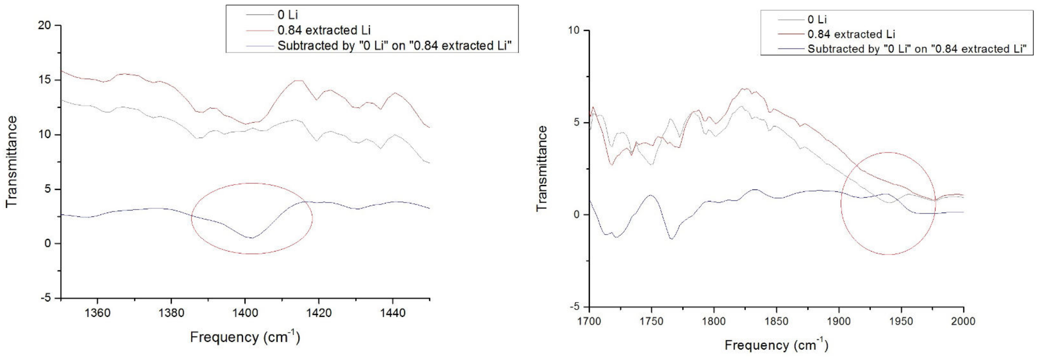

3.2.5 *Operando* XAFS

Operando XAFS was performed under the same conditions of other analogous tests, i.e. on a PTFE electrode, in the range $2 < E < 3.5$ V, adopting $LiPF_6$ in EC:PC:3DMC as electrolyte solution, and Li metal foil as anode. Active material mass load was about 15 mg/cm^2.

A Mössbauer *in situ* cell offers the appropriate geometry for such a technique, given that it works in transmission mode. However, a different type of separator is needed, as the common one, the Whatman® separator, contains some elements that absorb the desired radiation. Consequently, a Celgard® film was adopted, as it is about a polymeric film with neglectable absorption coefficient.

XAFS is a very useful technique to apply for *operando* tests. Several spectra can be collected throughout the cycling, without stopping the battery (Figure 3.36). Besides, it is about an element-selective and -tuning technique, so that spectra both for Cu and Fe can be recorded. Hence, the structural information can be gained by the two edges, independently, as already reported in literature even for a three-edge refinement [34].

XAFS experiment was conducted at ELETTRA Synchrotron Light Laboratory, in Basovizza (TS), at the XAFS beam line, as a part of the project # 20145337 ”Metal hexacyanoferrates-based cathodes for rechargeable batteries: structural and electronic studies by *operando* XAFS” (M. Giorgetti as principal investigator).

The data were recorded at Fe and Cu K-edges in transmission mode. The energies

FIGURE 3.36: Electrochemical curve. *Operando* XAFS

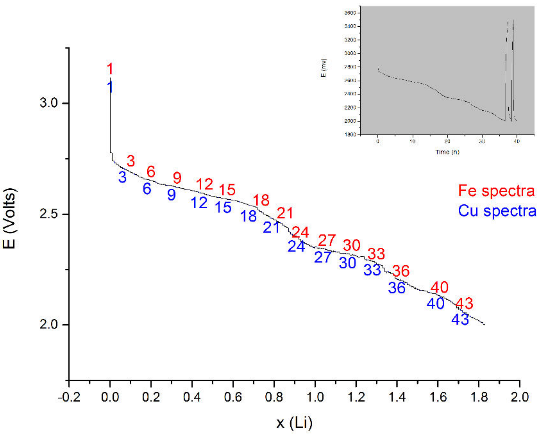

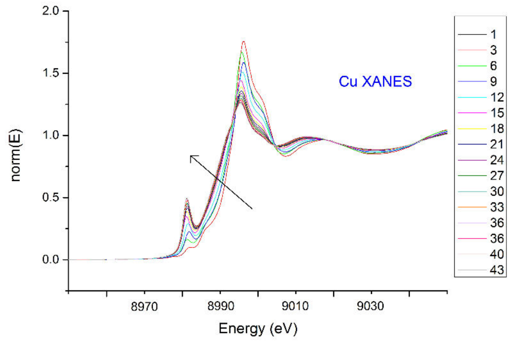

FIGURE 3.37: *Operando* XAFS. Cu XANES region

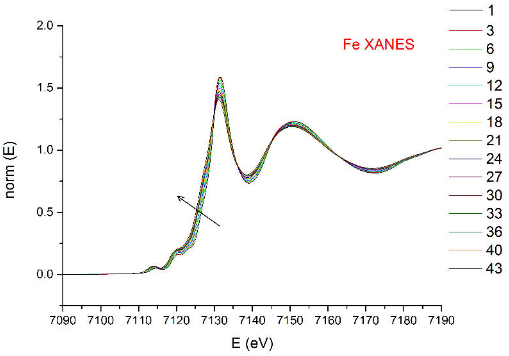

FIGURE 3.38: *Operando* XAFS. Fe XANES region

were defined by assigning the first inflection point of the spectra of the metallic iron and copper to 7112 eV and 8979 eV, respectively.

As shown in Figure 3.37, Cu K-edge dramatically changes, and it is evident that reduction from Cu(II) to Cu(I) occurs during the very first plateau. Not only the energy threshold shifts to lower energies (as expected, given that oxidation number decreases), but a pre-edge peak becomes also clearer, which is the characteristic feature of this monovalent ion.

Furthermore, no relatively big change occurs in the XANES region after the 18^{th} spectrum, that is at the end of the first plateau. We can assume that copper is mainly reduced in the first part of the discharge.

Fe XANES spectra are characterized by a pre-edge peak, due to transitions to bound states (corresponding to the 1s–3d transition) (Figure 3.38). Spectra do

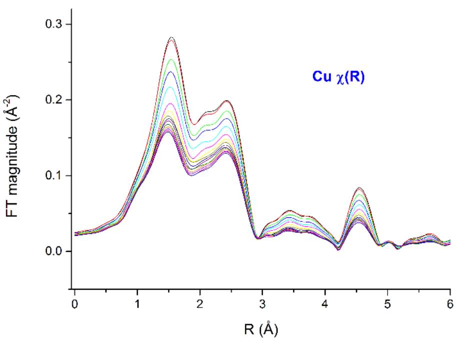

Figure 3.39: *Operando* XAFS. Cu Fourier-transformed EXAFS signal

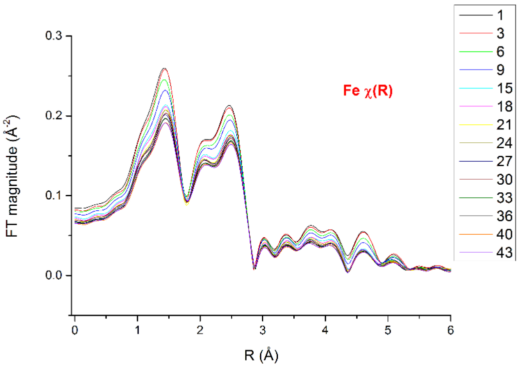

Figure 3.40: *Operando* XAFS. Fe Fourier-transformed EXAFS signal

not change much among cycling, implying that iron does not take place to the insertion process.

Concerning Fe K-edge, it shifts towards lower energies, as the discharge proceeds. That means that the energy to induce the expulsion of the photoelectron decreases during the reduction, but it is not related to a change in oxidation state.

The edge energy is in agreement with Mössbauer that asserts that iron is a divalent ion. However, by considering a high covalency, it would not be totally right to label iron as Fe(II) exactly. As a matter of fact, in literature [35] the average number of *d* electrons has been evaluated to be 5.39, for anisotropic electronic structure of the crystal that leaves ambiguity between a d^6 and d^5 configuration. Additional XANES experiments at high resolution may be performed to further investigate the pre-edge region.

According to the Fourier-transformed signal (Figure 3.39, 3.40), a continuous decreasing is displayed, meaning that structural disorder raises up. It may be a synthom of amorphisation and/or dissolution of the material into the electrolyte solution, perhaps even provoked by the reduction of copper.

While reduction took place in a appropriate way, oxidation did not work well, probably due to a decrease of electrical contact.

Conclusions and Perspectives

Research based on secondary cells is constantly growing up because of its importance in technology and application in hand-held consumer devices.

Cells with an excellent cyclability are sought, and performances are improved by changing operative conditions and materials: new cathodic materials are tested, above all those characterized by an open-framework structure, which allows a rapid insertion and extraction with little lattice strain; different electrolytes and solvents are used in combination with additives, in order to achieve a good ion-mobility and stability within the potential window; new anodic materials are researched to avoid hazards, without lowering performances meanwhile.

In this work, a study on a cathodic material has been carried out: different formulations have been evaluated, and not only lithium was adopted as anode, but also sodium, in order to take into account the concerns relative to lithium, and to explore an option, which is nowadays a growing alternative to Li-ion batteries.

Copper hexacyanoferrate has an excellent electrochemical behaviour, as confirmed by many authors: several cycles of discharge and charge are feasible with neglectable efficiency loss. Copper nitroprusside has been chosen for its characteristics, as it consists of a 3D framework with large channels and interstices, hence allowing theoretically discharge and charge processes, like copper hexacyanoferrate. The difference between them is a stronger anisotropy of copper nitroprusside, due to nitrosyl ligand. Since nitrosyl could undergo a redox, copper nitroprusside becomes an interesting candidate for a research work: more electroactive species imply a greater specific capacity, and if performances are high enough, it could be processed as cathode.

Copper nitroprusside has been synthesized with a low-cost and scalable method, that is co-precipitation. Different batches displayed a good reproducibility and the obtained yield is quite high, taking into consideration also that the method has not been optimized.

Characterization revealed the crystallinity of the compound and a $Imm4$ tetragonal structure with cell parameters a and c equal to 10.06 and 10.92 Å respectively, due to the Jahn-Teller distortion of copper (II). Mössbauer spectroscopy proved that iron is its (+2) oxidation state, and consequently that nytrosyl is in its oxidized form, i.e. the linear one.

As expected, there is a correspondence between cyclic voltammograms and electrochemical curves: actually, different insertion and extraction potentials match with the extracted redox potentials in CVs. This means that processes of insertion and extraction are due to redox phenomena, as they must involve a change in the oxidation state of the host compound. According to voltammograms, the compound is not able to undergo reversibly the reductions that take place in the first discharge; although such an irreversibility is clear even in electrochemical tests, the material is able to cycle yet.

Electrochemical tests were done both with a PTFE- and a CMC-based formulation.

Regarding PTFE-based electrodes, both $LiPF_6$ and LiTFSI were adopted as electrolyte, at a C/20 rate: a higher specific capacity was obtained with LiTFSI, even if the absolute amount of inserted/extracted Li-equivalents was on average greater for $LiPF_6$, which exhibited cycles between roughly 0.5 Li. Both for these two formulations, a quite high capacity fading is recorded among cycles (Figure 3.41).

CMC-formulation gave unexpected results, as it provided more stable performances overall: specific capacity resulted smaller in the first cycle, but its fading is little compared to PTFE-formulation. The absolute amount of inserted/extracted Li-equivalents was lower, yet. However, CMC-based electrode was cycled at a C/10 rate, that is twice faster than PTFE-electrodes. For this reason, CMC-formulation could be the ideal one, probably due to the more homogeneous dispersion of active material.

FIGURE 3.41: Formulations comparison and relative performances

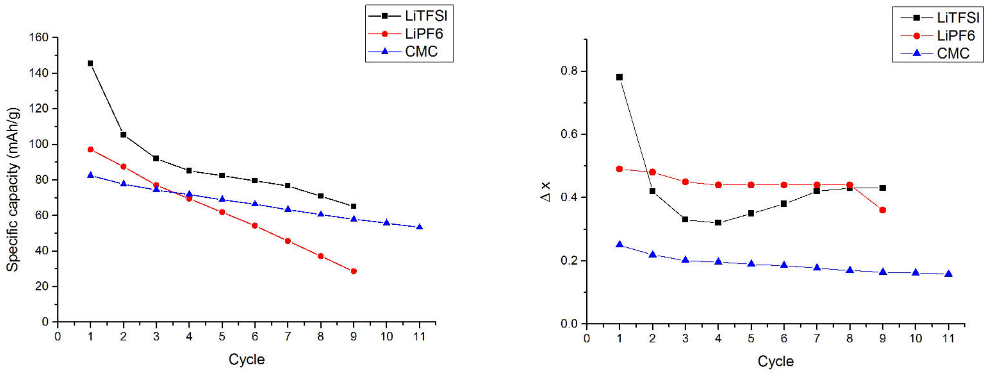

Even though CMC-formulation provided better performances, these are not competitive at all to those of other cathodic materials, for instance copper hexacyanoferrate. It could be used in a primary cell, given that it was able to insert even more than 2 Li-equivalents, but specific capacity would be still small compared to other primary cells.

In order to investigate the insertion process, *operando* tests were employed and compared (Figure 3.42). *Operando* XRD highlighted a long range disordering among reduction, while *operando* XAFS a short range one: for this reason, an amorphisation occurs. Besides, even if an amorphisation takes place, the material is able to cycle: that means that the insertion process may be a *conversion* one, i.e. passing through an amorphisation and swinging between two states, which differ from the original one.

A striking point concerning *operando* XRD is that peak decreasing (16.2°, 17.6°) and new peaks arising (23.3°) start approximatively after the very first plateau, that is after copper reduction.

Operando Mössbauer displayed a lowering in the signal, suggesting a dissolution of the material, while *operando* IR may confirm the theory that the nitrosyl group is gradually reduced: in case of a reduction of this ligand, physical properties may change, and dissolution may occur also because of copper reduction, modifying at the same time long- and short-range order.

Further works could be focused on a new cathodic material with a nitrosyl ligand,

FIGURE 3.42: *Operando* techniques comparison

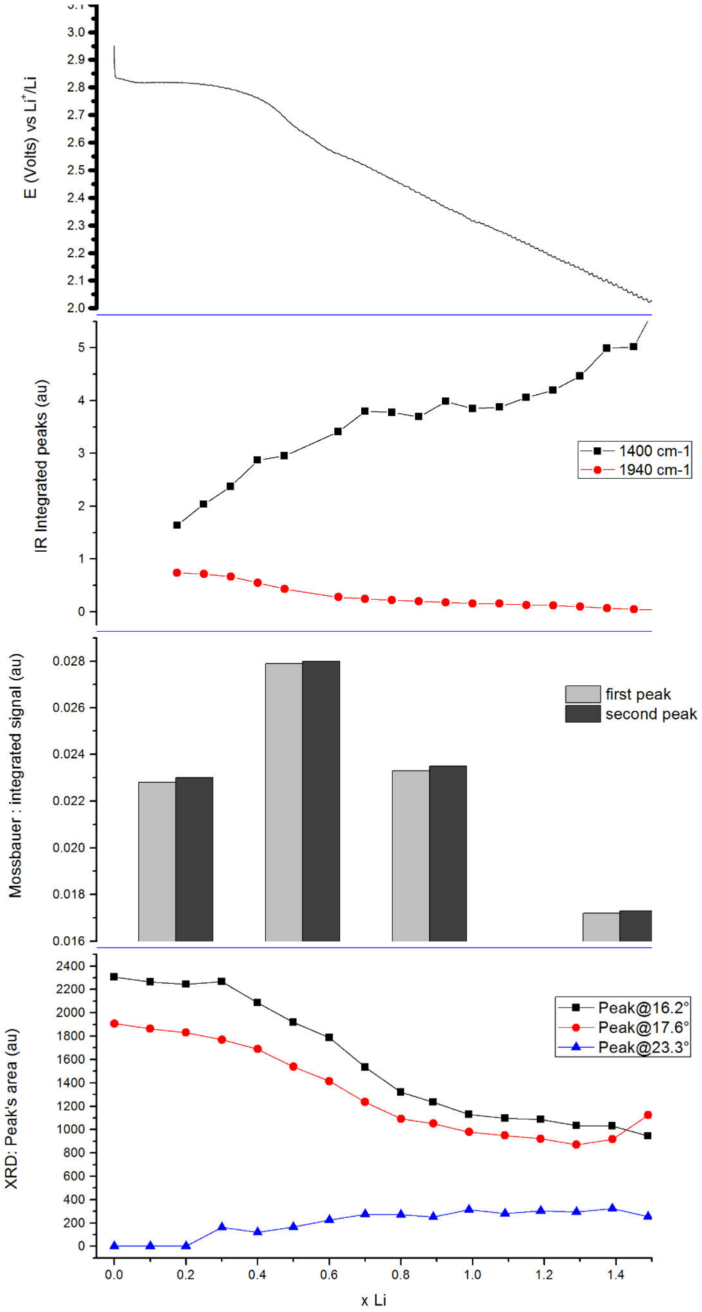

but characterized by a more stable electrochemical behaviour. Distorted Cu(II) may be replaced by another transition metal, such as Fe(II) or Co(II), and further tests could be done both with PTFE and CMC as binder, using different solvent mixtures in order to achieve a good viscosity and ion-mobility.

Speaking of open-framework materials, an Al-containing ion may be inserted in and extracted from such compounds: Al-ion electrolytes and solvents could be studied and optimized in order to reach good performances. As aluminium batteries offer a great energy density, they could be investigated; moreover, aluminium batteries suffer from cathode disintegration, so that such host materials could represent a possible solution.

Appendix A

A brief introduction to Mössbauer spectroscopy [2]

Mössbauer spectroscopy is based on the Mössbauer effect, i.e. the recoilless nuclear resonance absorption of γ rays.

The Mössbauer effect has been detected for 72 isotopes of 42 different elements. Suitable lifetime of nuclear excited state, transition energy, easy accessibility and handling are important criteria for this spectroscopic technique, so that just 20 elements can be studied by Mössbauer, e.g. iron, tin, antimony, tellurium, iodine, gold, nickel, ruthenium, iridium, tungsten, krypton, xenon, many of the rare earth elements, neptunium. The most studied nuclide is ^{57}Fe.

Radioactive ^{57}Co with 270 days halflife is exploited as the γ radiation source for ^{57}Fe Mössbauer spectroscopy. ^{57}Co decays by electron capture (EC) from K-shell, reducing the proton number from 27 to 26, corresponding to ^{57}Fe.

Generically, a nucleus with Z protons and N neutrons in a nuclear excited state of energy E_e undergoes transition to the ground state of energy E_g by emitting a γ quantum of energy E_e–E_g. The γ quantum may be absorbed by another nucleus of the same kind (same Z and N) in its ground state, leading the nucleus to an excited state (*resonant absorption*). The subsequent transition to the ground state of the latter emits either a conversion electron e^- or a γ quantum (*resonant fluorescence*), as schematically reported in figure A.1.

Figure A.1: Representation of Mössbauer effect (resonant absorption) and nuclear resonant fluorescence

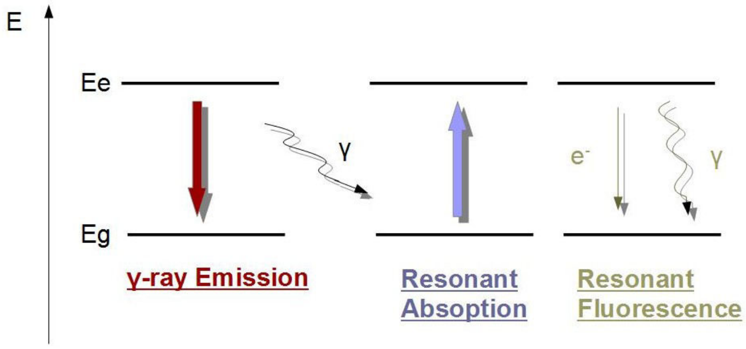

An excited state of mean lifetime τ does not have a singular energy value. On the contrary, the energy spaces in an interval of width ΔE according to the Heisenberg principle of uncertainty:

$$\Delta E \cdot \Delta t \geq h/2\pi \tag{A.1}$$

where h is the Planck constant and Δt, the time needed to measure ΔE, is comparable to τ.

A nuclear transition from an excited state to the ground state involves in fact different transitions, centred around the most probable energy E_0, with a spectral width so expressed:

$$\Gamma \cdot \tau = h/2\pi \tag{A.2}$$

where $\Gamma = \Delta E$ is the full width of the spectral line at half maximum. The higher the mean lifetime, the broader the line.

In Mössbauer spectroscopy a precise range of mean lifetime is required, being the optimal interval $10^{-11} \leq \tau \leq 10^{-6}$ s. Just some lifetimes are suitable because of the required overlap between the source and the absorber in a Mössbauer experiment.

Actually, the maximum resonance absorption takes place if the emission and absorption lines are placed at the same energy $E_0 = E_e - E_g$.

When the γ photon with mean energy E_0 is emitted from the nuclide, which is supposed to be at rest, a recoil is imparted to the nucleus, which moves in opposite direction to the direction of γ ray emission:

$$E_R = 1/2m \cdot v^2 \tag{A.3}$$

being E_R the kinetic recoil energy, m the nucleus mass and v the velocity. Therefore, calling E_γ the energy of the emitted photon:

$$E_\gamma = E_0 – E_R \tag{A.4}$$

being E_R small compared to E_0.

For this reason, the emission line is displaced by an amount E_R from the position E_0. During the absorption, the gamma-photon to be absorbed by the nucleus requires the total energy $E_\gamma = E_0 + E_R$, taking into consideration the energy gap from the ground to the excited state and the recoil effect, so that the emission and absorption lines are separated by $2E_R$, which is 106 times greater than the natural width Γ.

Overlap between the two transition lines is not possible for isolated atoms or molecules in the gaseous or liquid state. In the solid state a Mössbauer active atom is rigidly bound to the lattice, so that the recoil energy is much lowered and mostly transferred to the lattice vibrational system. The decaying atom will remain in such a way in the same position and the transferred energy will heat the near surroundings.

For nuclear resonance absorption of gamma-ray to be successful, one must bring the emission and the absorption lines at the same energy mean value or at least get a partial overlap, by making use of the Doppler effect to compensate for the recoil energy loss. For this reason, the source and the absorber are moved relative to each other and the Mössbauer spectrum exhibits the relative transmitted signal as a function of the Doppler velocity.

One thing to keep in mind is that nuclei are positively charged and may have nuclear moments, which interact with the electric and magnetic fields and perturb the nuclear energy levels, originating the so-called nuclear $hyperfine\ interactions$. For instance, electrons with zero-angular momentum (s-electrons) can penetrate the nucleus and spend a fraction of time inside it: this electrostatic perturbation can shift nuclear energy levels without changing the degeneracy. This shift is denoted as isomer shift δ, which gives information about oxidation state, spin state, and bonding properties.

Isomer shift is a Mössbauer parameter, such as *quadrupole splitting* ΔE_Q and *magnetic splitting* ΔE_M, which derive from an interaction with an electric and magnetic field, respectively. Quadrupole splitting reveals something about oxidation state, spin state and site symmetry, while magnetic splitting provides info on the magnetic properties. Taking into account all these parameters, it is possible to handle a powerful and really sensitive tool.

Appendix B

A brief introduction to XAFS spectroscopy [3] [4] [5]

X-Ray Absorption Fine Structure (XAFS) is a quantum mechanical phenomenon based on the photoelectric effect: when an X-ray phonon of appropriate energy is absorbed by an atom, an inner shell electron is freed into the continuum and a *core* hole is left behind.

XAFS experiment measures the absorption coefficient μ as a function of energy E: as E increases, μ generally decreases ($\mu \propto E^{-3}$), that is matter becomes more transparent and X-rays more penetrating, save for some discontinuities, where μ rapidly rises up. These exceptions correspond to particular energies, the so-called *absorption edges* E_0, characteristic of the material, where the amount of energy exactly matches the *core* electron binding energy.

XAFS could be regarded as constituted of pre-edge and edge regions (XANES = X-ray Absorption near Edge Spectroscopy) and a post-edge region (EXAFS = Extended X-Ray Absorption Fine Structure), which is extended up to 1000 eV above the absorption edge.

A striking features of XAFS is that this technique can be applied to all states of matter, and for both crystalline and amorphous materials, which makes XAFS a powerful tool for several sciences. XAFS is even element selective, as specific transitions take place, and element tunable, since absorption edges of next elements are sufficiently spaced.

The measured quantity, μ (cm^{-1}), is the linear absorption coefficient, and is defined as the the fraction of a beam of radiation absorbed per unit thickness of absorber. Normalization to the density of the material results quite convenient, as different states of matter may be analysed: the mass absorption coefficient μ_m (cm^2/g) is the linear absorption coefficient divided by the density of the absorber.

$$\mu \cdot x = \ln I_0/I \tag{B.1}$$

$$(\mu/\rho) \cdot \rho \cdot x = \ln I_0/I \tag{B.2}$$

being x the sample length (cm), I_0 the incident beam, I the transmitted beam, ρ the density (g/cm^3).

X-ray radiation is ionizing, and the absorbing atom turns to an excited ion after the electron liberation. Relaxation may occur in two different ways: (i) the *core* hole may be filled by a higher-energy electron and the energy difference is released as a second phonon, whose energy is smaller compared to that of the primary absorption, for an inner transition occurs; or (ii) an Auger *secondary* electron may be freed, after having absorbed the second phonon.

For energies lower than the absorption edge, an inner transition from an inner shell to a partially occupied or unoccupied state may occur, while more energetic radiations impart to the photoelectron enough kinetic energy, so that it behaves like a wave and can interact with the potential of neighbouring atoms, giving rise to scattering events.

The XANES region is sensitive to the element type and to many other factors, such as the oxidation state, the electronic configuration, and the local geometry around the photoabsorber. For instance, as the effective charge on an atom increases, E$_0$ shifts to higher energies, since the binding energy for a *core* shell electron is greater. Moreover, pre-edge transitions depend on the spin state: in case of a d^6 configuration and an octahedral geometry, d orbitals are split, so that 3 t_{2g} orbitals are lower in energy respectively to the other 2 e_g orbitals. For a low spin state, just one transition from the *core* shell to the d orbitals is allowed, while for a high spin state, two different transitions may take place, the first one to a partially occupied t_{2g}, the second one to a likewise partially occupied e_g orbital.

Conversely, EXAFS region gives important structural information, determining the environment of an atom, that is coordination number and type of neighbouring atoms, in addition to interatomic distances and structural and/or thermal disorder.

The EXAFS signal is commonly described by a wave with a given amplitude and phase, which in first approximation depend on coordination number and type of atoms, and on distances, respectively.

The EXAFS signal is so expressed:

$$\chi(E) = \frac{\mu(E) - \mu_0(E)}{\Delta\mu_0(E)} \tag{B.3}$$

where $\chi(E)$ is the EXAFS signal, $\mu(E)$ is the sample absorption, $\mu_0(E)$ is the absorption of the bare atom, as if it were without coordination sphere, $\Delta\mu_0(E)$ is the edge jump.

In this way the signal is compared to the bare atom and normalized to a single absorption event.

XAFS stands for a bulk technique able to study different kind of materials, to be element selective, and to search for low concentration absorbers. Besides, a synchrotron radiation source can be used in order to increase S/N ratio.

Bibliography

[1] J. B. Leriche, S. Hamelet, J. Shu, M. Morcrette, C. Masquelier, G. Ouvrard, M. Zerrouki, P. Soudan, S. Belin, E. Elkaim, and F. Baudelet, "An Electrochemical Cell for Operando Study of Lithium Batteries Using Synchrotron Radiation," *Journal of The Electrochemical Society*, vol. 157, no. 5, p. A606, 2010.

[2] P. Gütlich, R. Link, and A. Trautwein, *Mössbauer spectroscopy and transition metal chemistry.* 2011.

[3] G. Vlaic and L. Olivi, "EXAFS Spectroscopy : a Brief Introduction," *Croatica Chemica Acta*, vol. 77, no. 3, pp. 427–433, 2004.

[4] M. Giorgetti, "Review Article A Review on the Structural Studies of Batteries and Host Materials by X-Ray Absorption Spectroscopy," *ISRN Materials Science*, vol. 2013, 2013.

[5] G. Bunker, *Introduction to XAFS: A Practical Guide to X-ray Absorption Fine Structure Spectroscopy.* 2010.

[6] V. Colin and B. Scrosati, *Modern Batteries.* 1997.

[7] M. Armand, "Issues and challenges concerning lithium batteries," *Nature*, vol. 414, no. November, pp. 359–367, 2001.

[8] T. M. Bandhauer, S. Garimella, and T. F. Fuller, "A Critical Review of Thermal Issues in Lithium-Ion Batteries," *Journal of The Electrochemical Society*, vol. 158, no. 3, p. R1, 2011.

[9] R. W. Schmitz, P. Murmann, R. Schmitz, R. Müller, L. Krämer, P. Isken, P. Niehoff, S. Nowak, G. V. Röschenthaler, N. Ignatiev, P. Sartori, S. Passerini, M. Kunze, A. Lex-Balducci, C. Schreiner, I. Cekic-Laskovic, and M. Winter, "Investigations on novel electrolytes, solvents and SEI additives for use in lithium-ion batteries: Systematic electrochemical characterization and detailed analysis by spectroscopic methods," *Progress in Solid State Chemistry*, vol. 42, no. 4, pp. 65–84, 2014.

[10] R. Ruffo, C. Wessells, R. a. Huggins, and Y. Cui, "Electrochemical behavior of LiCoO2 as aqueous lithium-ion battery electrodes," *Electrochemistry Communications*, vol. 11, no. 2, pp. 247–249, 2009.

[11] M. Dahbi, F. Ghamouss, F. Tran-Van, D. Lemordant, and M. Anouti, "Comparative study of EC/DMC LiTFSI and LiPF6 electrolytes for electrochemical storage," *Journal of Power Sources*, vol. 196, no. 22, pp. 9743–9750, 2011.

[12] S. S. Zhang, "A review on electrolyte additives for lithium-ion batteries," *Journal of Power Sources*, vol. 162, no. 2 SPEC. ISS., pp. 1379–1394, 2006.

[13] J. C. Pramudita, S. Schmid, T. Godfrey, T. Whittle, M. Alam, T. Hanley, H. E. A. Brand, and N. Sharma, "Sodium uptake in cell construction and subsequent in operando electrode behaviour of Prussian blue analogues, Fe[Fe(CN)6]1-x·yH2O and FeCo(CN)6.," *Phys. Chem. Chem. Phys.*, vol. 16, no. 44, pp. 24178–24187, 2014.

[14] D. Kundu, E. Talaie, V. Duffort, and L. F. Nazar, "The Emerging Chemistry of Sodium Ion Batteries for Electrochemical Energy Storage," *Angewandte Chemie International Edition*, no. 150, pp. n/a—-n/a, 2015.

[15] M.-C. Lin, M. Gong, B. Lu, Y. Wu, D.-Y. Wang, M. Guan, M. Angell, C. Chen, J. Yang, B.-J. Hwang, and H. Dai, "An ultrafast rechargeable aluminium-ion battery," *Nature*, 2015.

[16] S. Liu, G. L. Pan, G. R. Li, and X. P. Gao, "Copper hexacyanoferrate nanoparticles as cathode material for aqueous Al-ion batteries," *J. Mater. Chem. A*, vol. 3, no. 3, pp. 959–962, 2014.

[17] M. Ware, "Prussian Blue: Artists' Pigment and Chemists' Sponge," *Journal of Chemical Education*, vol. 85, no. 5, p. 612, 2008.

[18] N. R. De Tacconi, K. Rajeshwar, and R. O. Lezna, "Metal hexacyanoferrates: Electrosynthesis, in situ characterization, and applications," *Chemistry of Materials*, vol. 15, no. 16, pp. 3046–3062, 2003.

[19] H. J. Buser, D. Schwarzenbach, W. Petter, and a. Ludi, "The crystal structure of Prussian Blue: Fe4[Fe(CN)6]3.xH2O," *Inorganic Chemistry*, vol. 16, no. 11, pp. 2704–2710, 1977.

[20] M. Giorgetti, D. Tonelli, M. Berrettoni, G. Aquilanti, and M. Minicucci, "Copper hexacyanoferrate modified electrodes for hydrogen peroxide detection as studied by X-ray absorption spectroscopy," *J. Solid State Electrochem.*, vol. 18, no. 4, pp. 965–973, 2013.

[21] L. Guadagnini, D. Tonelli, and M. Giorgetti, "Improved performances of electrodes based on Cu2+-loaded copper hexacyanoferrate for hydrogen peroxide detection," *Electrochimica Acta*, vol. 55, no. 17, pp. 5036–5039, 2010.

[22] M. Giorgetti, L. Guadagnini, D. Tonelli, M. Minicucci, and G. Aquilanti, "Structural characterization of electrodeposited copper hexacyanoferrate films by using a spectroscopic multi-technique approach," *Physical Chemistry Chemical Physics*, vol. 14, no. 16, p. 5527, 2012.

[23] H. Tokoro and S.-i. Ohkoshi, "Novel magnetic functionalities of Prussian blue analogs.," *Dalton transactions (Cambridge, England : 2003)*, vol. 40, no. 26, pp. 6825–6833, 2011.

[24] J. Jiménez-Gallegos, J. Rodrýguez-Hernández, H. Yee-Madeira, and E. Reguera, "Structure of porous copper prussian blue analogues: Nature of their high H2 storage capacity," *Journal of Physical Chemistry C*, vol. 114, no. 11, pp. 5043–5048, 2010.

[25] C. D. Wessells, R. a. Huggins, and Y. Cui, "Copper hexacyanoferrate battery electrodes with long cycle life and high power.," *Nature Commun.*, vol. 2, p. 550, 2011.

[26] J. P. Souza and D. R. Silvestrini, "Direct Preparation and Characterization of Copper Pentacyanonitrosylferrate Nanoparticles," *Journal of nanomaterials*, vol. 2015, 2015.

[27] A. B. Nikolskii, N. B. Batalova, and Y. I. Dyachenko, "Study of the nature of M-NO bond in nitroso complexes," *Teoeticheskaya i Eksperimental'naya Khimiya*, vol. 15, no. 2, pp. 153–156, 1979.

[28] Brown, "Nitrogen and Oxigen bonded Nitrosyl. Metal coplexes of the nitroprusside ion.," *Inorg. Chem.*, vol. 14, no. 10, pp. 2582–2584, 1975.

[29] M. D. Carducci, M. R. Pressprich, and P. Coppens, "Diffraction studies of photoexcited crystals: Metastable nitrosyl-linkage isomers of sodium nitroprusside," *Journal of the American Chemical Society*, vol. 119, no. 11, pp. 2669–2678, 1997.

[30] P. Coppens, I. Novozhilova, and A. Kovalevsky, "Photoinduced linkage isomers of transition metal nitrosyl compounds and related complexes," *Chemical Reviews (Washington, D. C.)*, vol. 102, no. 4, pp. 861–883, 2002.

[31] A. Gomez, J. Rodriguez-Hernandez, and E. Reguera, "Unique coordination in metal nitroprussides: The structure of Cu[Fe(CN)5NO].2H2O and Cu[Fe(CN)5NO]," *J. Chem. Crystallogr.*, vol. 34, pp. 893–903, Dec. 2004.

[32] A. C. de Sá, L. L. Paim, U. D. O. Bicalho, and D. R. do Carmo, "Determination of N-acetylcysteine by cyclic voltammetry using modified carbon paste electrode with copper nitroprusside adsorbed on the 3-aminopropylsilica," *International Journal of Electrochemical Science*, vol. 6, no. 9, pp. 3754–3767, 2011.

[33] L. Reguera, J. Balmaseda, C. P. Krap, and E. Reguera, "Hydrogen storage in porous transition metals nitroprussides," *Journal of Physical Chemistry C*, vol. 112, no. 28, pp. 10490–10501, 2008.

[34] M. Giorgetti and M. Berrettoni, "Structure of Fe/Co/Ni hexacyanoferrate as probed by multiple edge X-ray absorption spectroscopy," *Inorganic Chemistry*, vol. 47, no. 13, pp. 6001–6008, 2008.

[35] Y. Nanba, D. Asakura, M. Okubo, H. Zhou, K. Amemiya, K. Okada, P.-A. Glans, C. A. Jenkins, E. Arenholz, and J. Guo, "Anisotropic charge-transfer effects in the asymmetric Fe(CN)5NO octahedron of sodium nitroprusside: a soft X-ray absorption spectroscopy study.," *Phys. Chem. Chem. Phys.*, vol. 16, no. 15, pp. 7031–7036, 2014.